



Subseasonal prediction of springtime Pacific-North American transport using upper-level wind forecasts

John R. Albers^{1,2}, Amy H. Butler³, Melissa L. Breeden³, Andrew O. Langford³, George N. Kiladis²

¹Cooperative Institute for Research in the Environmental Sciences, University of Colorado Boulder, Boulder, 80305, USA

5 ²Physical Science Laboratory, NOAA Earth System Research Laboratory, Boulder, 80305, USA

³Chemical Science Laboratory, NOAA Earth System Research Laboratory, Boulder, 80305, USA

Correspondence to: John R. Albers (john.albers@noaa.gov)

Abstract. Forecasts of Pacific jet variability are used to predict stratosphere-to-troposphere transport (STT) and tropical-to-extratropical moisture exports (TME) during boreal spring over the Pacific-North American region. A retrospective analysis
10 first documents the regionality of STT and TME for different Pacific jet patterns. Using these results as a guide, Pacific jet hindcasts, based on zonal-wind forecasts from the European Centre for Medium-Range Weather Forecasting Integrated Forecasting System, are utilized to test whether STT and TME over specific geographic regions may be predictable for subseasonal forecast leads (3-6 weeks ahead of time). Large anomalies in STT to the mid-troposphere over the North Pacific, TME to the west coast of the United States, and TME over Japan are found to have the best potential for subseasonal
15 predictability using upper-level wind forecasts. STT to the planetary boundary layer over the intermountain west of the United States is also potentially predictable for subseasonal leads, but likely only in the context of shifts in the probability of extreme events. While STT and TME forecasts match verifications quite well in terms of spatial structure and anomaly sign, the number of anomalous transport days is underestimated compared to observations. The underestimation of the number of anomalous transport days exhibits a strong seasonal cycle, which becomes progressively worse as spring progresses into summer.

20 **1 Introduction**

Mass transport is important to many aspects of Pacific-North American climate, including: stratosphere-to-troposphere transport (STT) of ozone to the planetary boundary layer, which has negative impacts on human health (Fiore et al. 2003; EPA US 2006; Langford et al. 2009; Lefohn et al. 2011); STT to the free troposphere, which is needed to estimate the North American background distribution of ozone (Fiore et al. 2014, Cooper et al. 2015, Young et al. 2018); and water vapor
25 transport, which contributes to precipitation variability (Ralph and Dettinger 2011; Mahoney et al. 2016; Guan et al. 2015; Gershunov et al. 2017). Because of these impacts, identifying time periods when transport forecasts might be skillful on subseasonal timescales (forecasts 3-6 weeks into the future) is recognized as having high societal value (e.g., Lin et al. 2015; Baggett et al. 2017 and references therein).



30 Skillful subseasonal transport forecasts hinge, in large part, on the skillful prediction of atmospheric teleconnections (Baggett
et al. 2017; DeFlorio et al. 2019). Initial studies of subseasonal teleconnection variability suggested that enhanced predictability
might occur during spring when strong El Niño-Southern Oscillation (ENSO) conditions are present (Barnston 1994;
Branković et al. 1994; Branković and Palmer 1997). However, more recent studies suggest that, overall, teleconnections (Wang
and Robertson 2019) and transport (DeFlorio et al. 2019) on subseasonal timescales tend to be most predictable during winter,
35 though precipitation forecasts over the Pacific Northwest exhibit elevated skill during spring (Wang and Robertson 2019).
These results are not necessarily in conflict though, because the seasonal cycle of Pacific teleconnection patterns between
winter and summer are very sensitive to the location and scale of tropical forcing (Newman and Sardeshmukh 1998; Barsugli
and Sardeshmukh 2002). This suggests that during spring, year-to-year variability in the forecast signal-to-noise ratio (Kumar
et al. 2000, 2007; Sardeshmukh et al. 2000; Straus et al. 2003; Wu et al. 2006), and hence Pacific basin transport and circulation
40 forecast skill (Albers and Newman 2019), has the potential to be quite large. Nevertheless, even if teleconnections and transport
are more predictable during winter on average, predicting atmospheric circulation during spring is important in the context of
stratosphere-to-troposphere transport of ozone (Lefohn et al. 2011; Lin et al. 2015) and water vapor transport (Lee et al. 2014),
which together, motivate this study.

45 Stratosphere-to-troposphere transport and water vapor transport occur via distinct physical pathways. In midlatitudes, STT
occurs mainly via two mechanisms: stratospheric intrusions, which includes tropopause folds and potential vorticity streamers
(Reed and Danielson 1958; Hoerling et al. 1993; Langford and Reid 1998; Shapiro 1980); and transverse circulations in jet
exit regions (Langford et al. 1998; Langford 1999). Water vapor transport events, for example those embodied by so-called
'atmospheric rivers' (Zhu and Newell 1998), also arise via two distinct processes: long-range (Lagrangian) tropical-to-
50 extratropical moisture exports/transport (Stohl and James 2005; Bao et al. 2006; Knippertz and Wernli 2010; Knippertz et al.
2013); and extratropical transport related to local frontal dynamics (Newman et al. 2012; Madonna et al. 2014; Pfahl et al.
2014). In this study, we focus on spring season STT that extends downwards to the mid-troposphere and planetary boundary
layer (PBL), and long-range tropical-to-extratropical water vapor transports, hereafter referred to tropical moisture exports
(TME).

55 STT and TME have very different seasonal cycles in terms of timing and geography, which is readily observed in monthly
mean climatologies (Fig. 1; see Section 2 for a detailed description of STT and TME, which are both taken from the database
of Sprenger et al. 2017). Over western North America, STT of mass (and ozone) that reaches the PBL peaks in spring (Fig. 1,
left column; see also, Škerlak et al. 2014; Albers et al. 2018 and references therein). Despite the strong storm track located
60 over the North Pacific, deep STT is limited over the ocean due to a shallow marine boundary layer. In contrast, STT of mass
extending downwards into the middle troposphere (500 hPa), peaks during January and February and then slowly decreases
thereafter (Fig. 1, middle column). TME also undergoes a seemingly smooth transition during winter and spring, with an initial
peak extending from Hawaii to the western US during February, followed by a slow recession of transport westward, whereby



a secondary peak occurs near Japan during May (Fig. 1, third column; see also Knippertz and Wernli 2010; Mundhenk et al. 2016; Gershunov et al. 2017). The different regional and temporal characteristics of the STT and TME seasonal cycles shown in Fig. 1 are in part a reflection of the different physical processes that govern them, as outlined above. However, at least a portion of STT and TME seasonality and variability are linked by one important commonality: they are both directly modulated by large-scale Rossby waves (e.g., Ryoo et al. 2013; Albers et al. 2018), which themselves owe their propagation and breaking patterns to the strength and location of the subtropical and polar front jets (Hoskins and Ambrizzi 1993; Scott and Cammas 2002; Abatzoglou and Magnusdottir 2006; Hitchman and Huesmann 2007; Mundhenk et al. 2016; Olsen et al. 2019). For example, high TME is often observed on the western edge of blocking anticyclones in the North Pacific, where air is rising (Mundhenk et al. 2016), while STT occurs east of the block, where sinking air and stratospheric PV intrusions frequently develop (Sprenger et al. 2007). This means that the variability, and as we will show, the predictability, of both types of transport are dependent on the seasonal cycle of the Pacific jet.

Sometime between early March and late April, the Pacific jet undergoes a transition – which typically occurs very abruptly – from being strong and largely zonally contiguous between Asia and North America to being weak, with a discontinuity in the jet that spans most of the Pacific basin (Nakamura 1992; Newman and Sardeshmukh 1998; Hoskins and Hodges 2019; Breeden et al. 2020). The characteristics of this transition, and its relationship to forms of low-frequency variability that might be predictable on subseasonal timescales (e.g., ENSO) have been explored in the context of STT of mass and ozone. For example, Breeden et al. 2020 demonstrated that early season jet transitions (mid-to-late March), which are more common during La Niña conditions, are characterized by enhanced mass transport to the PBL (see also, Lin et al. 2015 and references therein). Conversely, late transitions (mid-to-late April) have weaker transport to the PBL although the association to El Niño is somewhat weaker. However, these analyses are retrospective, and it remains unclear whether forcings such as ENSO – and the resulting teleconnections – are actually forecast well enough to be useful when making subseasonal transport predictions.

While the predictability of mass transport on daily timescales is typically limited to less than two weeks (Lavers et al. 2016; DeFlorio et al. 2018), weekly averages of dynamical variables can occasionally have skill out to 3-6 weeks (e.g., Wang and Robertson 2019; Buizza and Leutbecher 2015; Albers and Newman 2019). This evokes the possibility that forecasts of atmospheric transport, which may be harder for models to explicitly predict on subseasonal timescales, might be successfully inferred from forecasts of more predictable or better constrained dynamical variables. Indeed, similar ideas have been successfully applied to assess the predictability of atmospheric blocking on seasonal timescales (Pavan et al. 2000) and precipitation on daily timescales (Lavers et al. 2014; Lavers et al. 2016). Here we assess the potential predictability of transport during spring based on the predictability of zonal wind variance associated with the Pacific jet. We do so by considering a very simple conditional probability: if 200 hPa zonal winds have a high (positive or negative) loading on a particular 200 hPa Pacific basin zonal wind pattern, then what will the corresponding shift in the probability of STT or TME be during those time periods? We first answer this question in the context of a retrospective analysis, which allows us to understand the regionality



of STT and TME for different jet patterns. Then, using the retrospective results as a guide, we utilize zonal wind hindcasts from the European Centre for Medium-Range Weather to test whether STT and TME over specific geographic regions may be predictable for subseasonal forecast leads (weeks 3-6). For both analyses, STT and TME are taken from the ETH-Zürich Feature-based climatology database (Sprenger et al. 2017), which allows us to apply a single, self-consistent measure of transport for both the retrospective (1979-2016) and hindcast (1997-2016) analysis periods.

2 Pacific jet and transport data

2.1 Jet variability

Jet variability over the Pacific-North American region is represented via empirical-orthogonal functions (EOFs), which are based on ERA-Interim (Dee et al. 2011) monthly mean (March-May, MAM) anomalies of 200 hPa zonal wind (cosine latitude weighted 10° - 70° N and 125° - 270° E) for the 1979-2016 period. Anomalies were created by removing the first four annual harmonics of the 1979-2016 daily climatology. Using monthly averages instead of daily or weekly values is motivated in part by the suggestion of Newman et al. (2012) that a large fraction of ocean-to-continent transport arises from low-frequency variability rather than individual synoptic events. Using monthly values also significantly boosts the variance explained by the leading three EOFs to nearly 60% versus <20% for daily values (e.g., Feldstein 2000). We use a bootstrap method to test for EOF degeneracy (North et al. 1982) and find that the first three EOFs (Fig. A1), which represent 25%, 21%, and 11% of the total MAM monthly mean wind variance, are reasonably well-separated and have robust spatial patterns (see Appendix for details). Hereafter we refer to the first three EOFs (and their corresponding PC time series) as EOF1 (PC1), EOF2 (PC2), and EOF3 (PC3).

While EOFs 1-3 are significantly correlated with several commonly used climate indices (Table 1), we make no inference that the EOF patterns represent dynamical or physical “modes” of the climate system (Monahan et al. 2009). Indeed, the significant correlations between each of our PC time series and multiple teleconnection indices indicates that the variance of our EOFs almost certainly results from a convolution of external forcing and internal variability across multiple timescales (e.g., Straus and Shukla 2002). Evidence for this assertion can be found by noting that while EOF1 is essentially uncorrelated with the NOAA Oceanic Niño Index (ONI) (correlation of 0.16 and not significant), EOF1 is one-month lag correlated with EOF2 (correlation 0.66, significance level >95%), which is itself highly correlated with the ONI index (correlation 0.78, significance level >95%). Thus, with one exception (considered in the Discussion) we simply use the EOFs as a data compression tool that helps to isolate the largest scale flow patterns that we anticipate will have the best chance for prediction.

To evaluate the potential predictability of Pacific jet variability, we use hindcasts (1997-2016) of 200 hPa zonal wind from the European Centre for Medium-Range Weather Forecasting Integrated Forecasting System (ECMWF IFS CY43R1/R3, model operational in 2017), which were obtained from the Subseasonal-to-Seasonal Prediction Project database (Vitart et al. 2017).



Hindcasts are ‘coarse-grained’ in time via a 7-day running-mean and in space via regrid-
130 longitude/latitude grid. Anomalies are computed by removing the lead dependent climatology, which also serves as a mean
bias correction (e.g., Buizza and Leutbecher 2015; Monhart et al. 2017). Hindcasts are computed as three-week averages for
weeks 3-5 (i.e., days 15-35). The 3-week averages are then projected onto the EOF patterns described above. We also computed
results for other averaging periods including weeks 3-4 and 3-6, as well as individual week 3, 4, and 5 forecasts, but settled on
135 weeks 3-5, because we found this window provided the best balance between predictability (averaging longer periods typically
extends the ‘forecast skill horizon’, e.g., Younas and Tang 2013; Buizza and Leutbecher 2015) versus extending the forecast
window out all the way to week 6 where there is very little amplitude remaining in the forecasts. The IFS hindcast PC time
series are verified against ERA-Interim-based PC time series prepared in an identical manner.

To help verify that the zonal wind EOF patterns are highlighting Pacific jet variability, we compare the EOFs to a upper
tropospheric jet stream climatology (Koch et al. 2006; Sprenger et al. 2017), which is itself based on ERA-Interim. The jet
140 climatology (1979-2014) is based upon vertical averaging of zonal and meridional winds between 100-500 hPa at every
horizontal grid point, where a ‘jet event’ at each grid point is detected when the vertically averaged wind exceeds 30 ms^{-1} . This
procedure yields a frequency of upper tropospheric jet ‘events’ at each grid point.

2.2 Transport composites

To examine stratosphere-to-troposphere mass transport and tropical-to-extratropical water vapor transport, we use three ETH-
145 Zürich Feature-based ERA-Interim Climatologies (Sprenger et al. 2017): a climatology of stratosphere-to-troposphere
transport to 500 hPa (STT_{500}), which provides an estimation of transport into the free troposphere; a climatology of
stratosphere-to-troposphere transport to the planetary boundary layer (STT_{PBL}) (Sprenger et al. 2003, Škerlak et al. 2014); and
a climatology of tropical-to-extratropical moisture/water vapor transport (TME), (Knippertz and Wernli 2010). The STT
climatologies (1979-2016) are based on Lagrangian parcel trajectories calculated using the LAGRANTO Lagrangian transport
150 model (Wernli and Davies 1997; Sprenger and Wernli 2015), where stratosphere-to-troposphere mass trajectories are
considered as exchange ‘events’ if they have 48-hour stratospheric, followed by 48-hour tropospheric, residence times. We
use both monthly mean and daily mean climatologies of STT_{500} and STT_{PBL} , all of which have units of number of mass
exchange events per 6-hourly time step. TME climatologies (1979-2016) are calculated via LAGRANTO water mass
trajectories that originate in the tropics and reach at least 35° N with a water mass flux greater than $100 \text{ g kg}^{-1} \text{ m s}^{-1}$; we use
155 monthly mean and daily mean TME climatologies where units are given as the number of TME events per 6-hourly time step.

For our retrospective transport analysis, we composite STT and TME for months when the zonal-wind PC time series were
larger than 1 STD. For the hindcasts, we use a slightly weaker 0.8 STD threshold in order to boost the number of samples
given the relatively short length of the subseasonal-to-seasonal hindcast database (1997-2016). We chose to keep the STD
threshold as high as possible though, because higher amplitude anomalies likely correspond to periods of higher forecast skill



160 (Compo and Sardeshmukh 2004; Van den Dool and Toth 1991; Johansson 2007). Importantly, the choice of threshold does
not qualitatively change the results. Hindcast transport composites are based on time periods when weekly average *forecasts*
of zonal-wind PC time series were predicted to exceed 0.8 STD. For hindcast verification composites, the composites are based
on periods when the *verification* weekly average zonal-winds PC time series exceeded 0.8 STD. This procedure typically
means that the verification composites include more samples because, as we will show, the weeks 3-5 IFS forecasts
165 systematically underestimate the amplitude of the zonal wind PC time series and thus do not exceed the STD threshold as often
as is observed.

While the original units of all of the ETH-Zürich climatologies are frequencies (jet frequency, STT, and TME), all of our
figures, except for the climatologies (Fig. 1), are presented in units of standard deviations. That is, for every variable, we
calculate anomalies from climatology and then divide by the anomaly standard deviation (z-scoring). Thus, a unit of ‘1 STD’
170 equates to a one standard deviation anomaly, where the standard deviation is calculated individually for each specific time
period considered (e.g., the STD normalization for a March monthly mean is different from the STD normalization used for a
three-week forecast period in March).

When comparing forecast and verification transport probability density functions (PDFs), we evaluate significance via a
combination of bootstrap confidence intervals (10,000 ensembles with replacement) and two-sample Kolmogorov-Smirnov
175 distribution tests (KS-test; Marsaglia et al. 2003; Hollander et al. 2013), where the later tests whether the shape and location
of two empirical distributions are significantly different. The PDFs themselves are created by taking box-area means of STT
or TME for a specified geographic region at every forecast time step and using each as a ‘sample’. The PDFs are then calculated
via kernel density estimation based on the collection of all samples for either the forecasts or verifications.

3 Results

180 3.1 Retrospective analysis

The first three EOF patterns of the 200 hPa zonal wind all exhibit anomalies that correspond to some amount of
extension/retraction and/or latitudinal shifting of the Pacific jet compared to climatology (Fig. 2). This interpretation is
confirmed by compositing ETH feature-based jet frequencies for time periods with high EOF loading (PC amplitude >1 STD),
which yields jet frequency distributions that correspond extremely well with each of the first three EOF wind patterns
185 (Supplementary Fig. S1). This suggests that the amount of wind variance explained by each of the individual EOFs is
sufficiently large that when the PC loading is high there are notable, vertically deep (at least 100-500 hPa), corresponding
shifts in the location of the Pacific jet stream. While the EOF patterns likely combine jet variability due to both the subtropical
and polar front jets (Koch et al. 2006), a strong jet stream of either type will act as a waveguide for Rossby waves (e.g.,



Schwierz et al. 2004; Rivière 2010 and references therein) with an increased frequency of STT and TME (e.g., Shapiro and
190 Keyser 1990, Koch et al. 2006).

To evaluate the jet-transport connection, we consider STT and TME for time periods with high zonal wind EOF loading
(absolute value of PCs>1 STD). Because the patterns of the STT and TME anomaly composites are so similar for both EOF
phases, we show only the positive EOF pattern; see Supplement Figs. S2-S4 for the negative phase. STT₅₀₀ maxima match the
195 EOF wind patterns quite well (Fig. 3, top row), with positive (negative) STT₅₀₀ anomalies tending to occur along the northern
flanks of the regions of stronger (weaker) winds (Koch et al. 2006), and hence increased (decreased) jet frequency. The
correspondence of higher STT₅₀₀ with higher windspeeds, suggests that transverse circulations around the jet play a key role
in transport, and confirms that the EOF-based STT₅₀₀ anomalies are related to variations in the North Pacific storm track
(Škerlak et al. 2014). STT_{PBL} on the other hand (Fig. 3 middle row), have maxima slightly downstream of the 500 hPa maxima,
200 which reflects the fact that deep STT tends to occur as maturing Rossby waves amplify and tropopause folds and potential
vorticity streamers extend downwards towards the surface (Wernli and Bourqui 2002; Sprenger et al. 2003, Appenzeller et al.
1996, Wernli and Sprenger 2007, Škerlak et al. 2015). Anomalous TME also corresponds well with the EOF patterns (Fig. 3,
bottom row), except that the anomalies are on the southern edge of the positive EOF wind patterns, which is due to the tendency
for strong TME to occur along the warm sector of a breaking Rossby wave (Bao et al. 2006; Knippertz et al. 2013).

205 While all of the transport composites are physically consistent with the EOF patterns, and hence jet variability, the STT₅₀₀ and
TME composites have a much more robust signal compared STT_{PBL}. That the STT_{PBL} is weaker is not entirely surprising
because while a high percentage of upper level breaking waves extend downwards to the mid- to upper troposphere,
subsequently causing associated STT₅₀₀ and TME, only a small subset of these waves will achieve the needed amplitude and
210 depth to extend all the way to the PBL. Moreover, transport to the STT_{PBL} is also dependent on the depth of the PBL, which
tends to be relatively shallow until late spring to early summer when convective heating begins to increase (Seidel et al. 2012;
Škerlak et al. 2014; Breeden et al. 2020). Nevertheless, all of the composites provide a basis for the expectation that Pacific
jet variability can be used as a predictor for transport over landmasses of interest, including the western United States, southern
Alaska, and Japan.

215 3.2 Potential predictability of jet shifts and transport

While subseasonal forecasts of teleconnection indices are known to exhibit reasonable correlation-based skill (Wang and
Robertson 2019), the amplitude of the anomalies is often quite weak compared to observations (Yamagami and Matsueda
2020). Thus, the relevant question here is, do forecast models predict jet variability well enough – in terms of both correlation
and amplitude – to provide guidance for subseasonal transport forecasting?

220



For weekly forecasts, the correlation between the forecasted and verified zonal wind PCs is ‘skillful’ (correlations >0.5 - 0.6 , Hollingsworth et al. 1980; Arpe et al. 1985; Murphy and Epstein 1989) within the deterministic timeframe (weeks 1-2) for all three EOFs (Table 2). Beyond week 2, however, the PC1 and PC3 correlations drop off rapidly, with the skill of predicting PC3 almost completely limited to synoptic timescales. On the other hand, PC2 retains useful skill all the way out to forecast
225 week 6, which may be due to its stronger relationship to ENSO (Table 1). These correlations suggest that only the first two PCs retain enough skill to be useful on subseasonal leads. The same result is true for the weeks 3-5 forecast window (Fig. 4), where forecast-verification correlations for both PC1 and PC2 are near or above 0.5, while PC3 exhibits very low correlation-based skill. In terms of the PC amplitudes of the weeks 3-5 forecasts, both PC1 and PC2 regularly exceed our 0.8 STD threshold, while the PC3 amplitude rarely exceeds it. Thus, while EOF3 is related to large transport anomalies over land regions
230 of interest (e.g., STT_{PBL} and TME over North America), it is unfortunately not predictable on subseasonal timescales (similar results are also found for EOFs 4 and higher). We therefore focus on predicting transport via PC1 and PC2.

The number of observed instances (verifications) when the PC1 and PC2 amplitudes exceeds 0.8 STDs exhibits a seasonal cycle (Fig. 5), though the degree of overlap of the confidence intervals suggests that the seasonal cycle is more pronounced
235 for EOF2 than for EOF1. The situation is a bit more complicated if the individual phases of each EOF are considered (see Supplement, Fig. S5), though the small sample sizes make conclusive inferences difficult. Nevertheless, the slow decay of observed PC1 and PC2 exceedances (i.e., large amplitude jet events) between March and May is qualitatively consistent with previous studies documenting the seasonality of jet activity and Pacific baroclinic wave amplitudes (Nakamura 1992; Koch et al. 2006). Unfortunately, the number of PC1 and PC2 exceedances predicted by the IFS at 3-5 week lead times has a much
240 stronger seasonal cycle compared to observations, with early spring having many more exceedances than for late spring for both phases of PC1 and PC2 (Fig. 5 and Supplement S5). This implies that the transport anomalies outlined next are more predictable, and hence the composites more heavily weighted, for the periods before the jet undergoes its spring transition (Newman and Sardeshmukh 1998; Breeden et al. 2020).

245 Based on the regions with the largest transport anomalies (Fig. 3) for the more predictable PC1 and PC2 time series (Fig. 4), we chose four subregions within the full Pacific domain to examine the potential predictability of STT and TME: EOF1-based STT_{500} for the North Pacific, which includes southern Alaska and the Russian Far East; EOF2-based STT_{PBL} for the western to intermountain-western US; EOF1-based TME for the western US; and EOF2-based TME for the West Pacific (Japan and far eastern Asia). These subregions are highlighted by the boxes in Figs. 6a, 7a, 8a, and 9a, respectively. To provide context
250 for the four subregion forecasts, we first show forecast and verification transport anomalies for the entire Pacific domain. For each of the four full domain figures (Figs. 6-9), the top two panels show verification transport composites, which are based on times when the *verification* zonal wind PC time series amplitude is greater than ± 0.8 STD (black lines in Fig. 4), while the bottom two panels show corresponding transport composites, except for time periods when the *forecasted* zonal wind PC time series amplitude is greater than ± 0.8 STD (orange lines in Fig. 4). For comparison, the months that are included in the



255 retrospective composites (Fig. 3) are highlighted by the light red and blue shading in Fig. 4 (note that the time periods when
the week 3-5 time series exceed the ± 0.8 STD threshold do not always match the red and blue shading regions, because the
shaded regions highlight periods when the monthly mean time series exceeded the monthly 1 STD threshold). The pattern
correlations between the forecast and verification transport composites for the full domains in Figs. 6-9 (not just for the boxed
in areas) are included in the forecast titles for both EOF phases. Transport predictability for the four boxed subregions is
260 subsequently evaluated via PDFs of transport for the forecasts and verifications (Fig. 10).

STT₅₀₀ based on the EOF1 forecast is qualitatively consistent with the verification-based composite for both positive and
negative EOF phases (Fig. 6), though the STT₅₀₀ pattern is better reproduced for the negative phase (pattern correlation of 0.49
vs. 0.75 for the positive vs. negative phases, respectively). In addition, the verification composites show an asymmetry between
265 opposite EOF1 phases in the amount of STT₅₀₀, which is also accurately forecasted, with the negative EOF phase exhibiting
peak values in the 0.75-1.25 STD range vs. 0.25-0.5 STDs for the positive EOF phase. This asymmetry is likewise reflected
in the forecast and verification PDFs of STT₅₀₀ for the North Pacific subregion (Fig. 10a), where the median for the positive
EOF1 phase is weakly negative, while the negative EOF1 phase has a greater than +0.5 STD median anomaly. The only
noteworthy difference between the North Pacific forecast and verification PDFs is that the forecast-based PDF is shifted
270 towards more positive values than the verification-based PDF. Regardless, the confidence intervals for the medians of the
positive vs. negative phases of the forecast-based PDFs are very well-separated and the underlying distributions are different
according to a KS-test, which suggests that the predicted shifts in transport are significant. We also evaluated forecasts of
STT₅₀₀ for various subregions over populated land masses (e.g., the western US), but the resulting verification and forecast
PDFs were not significantly different, which reflects the fact that STT₅₀₀ peaks over the North Pacific portion of the storm
275 track (Fig. 3a).

For EOF2-based STT_{PBL} over the western US, the verification composite is consistent with the retrospective composites (cf.,
Figs. 7a,b and Fig. 3e), however, the pattern is much weaker. One potential reason that the forecast and verification patterns
are weaker than in the retrospective analysis is the smaller time averaging window used when constructing the forecast and
280 verification composites (3 week averaging windows for the forecast/verification composites vs. 4 week averaging windows
for the retrospective composites). However, if the forecast averaging window is expanded to 4 weeks, fewer well-forecasted
periods are included in the composites, which also leads to a weaker STT_{PBL} pattern. Nevertheless, the forecast- and
verification-based STT_{PBL} composites (Fig. 7c,d) and PDFs for the western US subregion (Fig. 10b) do agree quite well, though
the STT_{PBL} distribution is notably shifted away from zero only for the negative EOF phase. The confidence intervals for the
285 medians overlap; thus, on average, the STT_{PBL} forecasts appear to be borderline in their usefulness. Still, the forecasted STT_{PBL}
do represent different distributions according to a KS-test, so the change in the shape of the tails of the distributions may be of
some practical use for prediction of extreme STT_{PBL} events.



The TME forecasts match the verifications very well, for both EOFs, and for both phases of each EOF, with basin-wide pattern
290 correlations ranging from 0.57 to 0.88 (Figs. 8-9). In addition, the magnitude of the anomaly values for both EOFs are notable,
with both TME phases exhibiting anomalies in the 0.5-1.25 STD range over relatively large portions of the Pacific domain.
Interestingly, positive TME centered over Alaska is predicted very well for the positive phase of EOF1 (Fig. 8a,c) and the
negative phase of EOF2 (Figs. 9b,d), yet it is unclear if this pattern represents a reliably predictable form of TME because
neither of the corresponding TME composites for the longer time record retrospective analysis show anomalies over Alaska
295 (cf., Figs. 8 and 9 to Figs. 3g and 3h, respectively). In contrast, the forecasted patterns of TME between Japan and the west
coast of the US (south of 55° N) are quite consistent with the jet (Figs. 1 and S1) and TME (Fig. 3, bottom row) patterns from
the retrospective analysis, which suggests that TME over broad regions of the Pacific basin may be reasonably predictable
during spring. Indeed, the western US and West Pacific subregion TME PDF shifts are robust and match the verification PDFs
very well (Fig. 10c and d, respectively). This is particularly true for the West Pacific where the median shift in TME transport
300 is nearly +/- 1 STD for each EOF phase, and the PDF forecast and verification PDFs are nearly identical.

Discussion and conclusions

Many ‘modes’ of climate variability are known to be associated with anomalous atmospheric transport. For example,
stratosphere-to-troposphere mass and ozone transport to the PBL over North America is known to be influenced by ENSO
(Breedon et al. 2020; Lin et al. 2015 and references therein), while the frequency of atmospheric rivers is thought to be
305 modulated by a variety of climate phenomena, including ENSO, the Madden-Julian oscillation, and the quasi-biennial
oscillation (Guan et al. 2012; Lee et al. 2014; Kim and Alexander 2015; Guan et al. 2015; Mundhenk et al. 2016; Guirguis et
al. 2019). However, retrospectively isolating such associations, which is equivalent to conducting a ‘perfect model’ forecast,
does not assure that current operational forecast models can successfully predict those relationships, particularly on
subseasonal timescales (e.g., Lavers et al. 2016; Baggett et al. 2017). Nevertheless, some teleconnection and transport patterns
310 appear to be potentially predictable on subseasonal timescales (e.g., Mundhenk et al. 2018; Wang and Robertson 2019; Pan et
al. 2019; DeFlorio et al. 2019; Yamagami and Matsueda 2020), though these forecasts are typically found to occur during
boreal winter.

Our analyses have shown that stratosphere-to-troposphere transport (STT) to at least 500 hPa and long-range tropical-to-
315 extratropical moisture transport (TME) over the Pacific-North American region can potentially be skillfully predicted on
subseasonal timescales (3-5 weeks ahead of time) during boreal spring. The transport forecasts themselves were inferred from
ECWMF IFS-based forecasts of Pacific jet variability. IFS Pacific jet forecasts for four Pacific-North American subregions
are associated with significant shifts in the probability of anomalous transport, including: STT into the free troposphere over
the North Pacific (Fig. 10a); STT into the planetary boundary layer over the intermountain-western US (Fig. 10b); TME over
320 the west coast of the US (Fig. 10c); and TME to Japan and far eastern Asia (Fig. 10d). While the forecasted shifts in transport



probability match verifications quite well, one deficiency is apparent: the IFS is able to predict the sign of the zonal wind PC time series with reasonable success (Table 2 and Fig. 4), yet it consistently struggles to maintain enough zonal-wind PC amplitude relative to the substantial weather-related noise (compare amplitude of forecast and verification time series in Fig. 4). This results in an underestimation of the number of anomalous transport days compared to observations (Fig. 5), which
325 degrades the estimation of the transport probabilities (Fig. 10).

The underestimation of the number of anomalous transport days exhibits a strong seasonal dependence, which becomes quite acute during April and May (Fig. 5). This implies that either overall teleconnection predictability decreases as spring proceeds, or alternatively, the IFS is simply unable to skillfully predict large amplitude jet anomalies with consistency beyond early-
330 spring. While it is beyond the scope of the current study to explore which one of these possibilities is responsible for the lack of consistent late spring skill, this is clearly an important question, because the first possibility would be a fundamental feature of the climate system, while the latter would be a model-based constraint that might theoretically be improved. Of course, these two possibilities are not mutually exclusive, because the increasing sensitivity of Pacific-North American teleconnections to tropical forcing at smaller spatial scales during the spring jet transition (Newman and Sardeshmukh 1998) may be inherently
335 less predictable, yet also more difficult to accurately model. That said, despite the IFS underestimation of the number of days with anomalously strong jet patterns (Fig. 5), the IFS is still able to identify roughly 15% (PC1) and 30% (PC2) of all spring days (March-May) that are anomalous, which suggests that using upper-level winds to forecast transport may currently be possible.

340 For the three types of transport that we have evaluated here, STT into the free troposphere and TME are the most robustly predicted, at least in terms of shifts of the average and extremes of their transport distributions (Fig. 10). STT to the PBL over the western US, on the other hand, mainly exhibits a change in the shape of the tails of the transport distributions, but a rather weak shift in the median (i.e., the shift of the medians of the two EOF2 phases have confidence intervals that are strongly overlapping, Fig. 10b). This has implications for the suggestion that ENSO may be used to predict air quality related to STT
345 of ozone during spring (e.g., Lin et al. 2015 and Albers et al. 2018 and references therein). Similar to previous retrospective analyses (e.g., Lin et al. 2015; Breeden et al. 2020), we find that mass transport to the PBL is associated with ENSO (Fig. 11), where here, we have composited STT_{PBL} based on periods when the NOAA ONI is greater than 0.8 STDs from the historical mean, which yields an equivalent number of samples to our EOF2-based results. The ONI-based (retrospective) transport composites look very similar to our earlier EOF2-based retrospective results (cf., Figs. 11a and b to Figs. 3e and S3c,
350 respectively. For proper comparison, note that PC2 and ONI are negatively correlated). Moreover, the transport PDFs for the intermountain-western US subregion based on PC2 versus ONI, for both ENSO phases, are drawn from the same distributions according to a two-sample Kolmogorov-Smirnov test (Fig. 11c). This close correspondence is due to the high correlation between the ONI and PC2 time series (Fig. 11d). Yet, because we have found STT_{PBL} predictions related to EOF2 to be significant only in terms of shifts in the tails of the distributions (cf. Fig. 10b and 11c), our results suggest that at best, ENSO



355 may be harnessed to provide STT_{PBL} forecast guidance on subseasonal timescales for extreme events only. Complicating
matters further in the context of ozone transport to the PBL (as opposed to simply mass transport as investigated here), is that
predictions based on ENSO will likely be even more difficult because STT of ozone is also modulated by the seasonal
variability of the available reservoir of ozone in the extratropical lower stratosphere (Neu et al. 2014; Albers et al. 2018). That
said, because it is doubtful that Nino-3.4-based indices like ONI capture the full dynamical scope of ENSO variability (Penland
360 and Matrosova 2006; Capotondi et al. 2015), the complete impact of ENSO on STT_{PBL} predictability certainly deserves further
study.

Data Availability

The ERA-Interim reanalysis data used in this study is available through the National Center for Atmospheric Research
Consortium for Atmospheric Research Data Archive: <https://rda.ucar.edu/>. The STT , TME, and jet ERA-Interim feature-based
365 climatology data is available from <http://eraiclim.ethz.ch/>. ECMWF IFS hindcast data is available via the S2S Prediction
Project (<http://s2sprediction.net/>).

Author Contributions

John R. Albers wrote retrospective and hindcast analysis code, created the figures, and wrote the manuscript. Amy H. Butler,
Melissa L. Breeden, Andrew O. Langford, and George N. Kiladis provided comments and edited the manuscript.

370 Competing Interests

The authors declare that they have no conflict of interest.

Acknowledgements

The authors would like to thank Michael Sprenger for graciously making the 6-hourly ETH Feature-based data available,
which made this study possible. JRA and AHB were funded in part by NSF grant #1756958. MLB was funded by NOAA
375 Climate and Global Change Postdoctoral Fellowship Program, administered by UCAR's Cooperative Programs for the
Advancement of Earth System Science (CPAESS) under award # NA18NWS4620043B. The authors would like to thank Yan
Wang for preparing the IFS S2S data and Benjamin Moore, who helped furnish the 6-hourly TME data.

References

380 Abatzoglou, J. T. and Magnusdottir, G.: Planetary wave breaking and nonlinear reflection: Seasonal cycle and interannual
variability, *J. Climate*, 19, 6139–6152, 2006.



- Albers, J. R. and Newman, M.: A priori identification of skillful extratropical subseasonal forecasts, *Geophys. Res. Lett.*, 46, 12 527–12 536, 2019.
- Albers, J. R., Perlwitz, J., Butler, A. H., Birner, T., Kiladis, G. N., Lawrence, Z. D., Manney, G. L., Langford, A. O., and Dias, J.: Mechanisms governing interannual variability of stratosphere-to-troposphere ozone transport, *J. Geophys. Res.*, 385 123, 234–260, 2018.
- Appenzeller, C., Davies, H., and Norton, W.: Fragmentation of stratospheric intrusions, *J. Geophys. Res.*, 101, 1435–1456, 1996.
- Arpe, K., Hollingsworth, A., Tracton, M., Lorenc, A., Uppala, S., and Kållberg, P.: The response of numerical weather prediction systems to FGGE level IIb data. Part II: Forecast verifications and implications for predictability, *Quart. J. R. Met. Soc.*, 111, 67–101, 1985. 390
- Baggett, C. F., Barnes, E. A., Maloney, E. D., and Mundhenk, B. D.: Advancing atmospheric river forecasts into subseasonal-to-seasonal time scales, *Geophys. Res. Lett.*, 44, 7528–7536, 2017.
- Bao, J., Michelson, S., Neiman, P., Ralph, F., and Wilczak, J.: Interpretation of enhanced integrated water vapor bands associated with extratropical cyclones: Their formation and connection to tropical moisture, *Mon. Wea. Rev.*, 134, 1063–1080, 2006. 395
- Barnston, A. G.: Linear statistical short-term climate predictive skill in the Northern Hemisphere, *J. Climate*, 7, 1513–1564, 1994.
- Barsugli, J. J. and Sardeshmukh, P. D.: Global atmospheric sensitivity to tropical SST anomalies throughout the Indo-Pacific basin, *J. Climate*, 15, 3427–3442, 2002.
- Branković, Č. and Palmer, T.: Atmospheric seasonal predictability and estimates of ensemble size, *Mon. Wea. Rev.*, 125, 859–874, 1997. 400
- Breeden, M. L., Butler, A. H., Albers, J. R., Sprenger, M., and O’Neil Langford, A.: The Spring Transition of the North Pacific Jet and its Relation to Deep Stratosphere-to-Troposphere Mass Transport over Western North America, *Atmos. Chem. Phys. Discuss.*, pp. 1–27, 2020.
- Buizza, R. and Leutbecher, M.: The forecast skill horizon, *Quart. J. R. Met. Soc.*, 141, 3366–3382, 2015. 405
- Capotondi, A., Wittenberg, A. T., Newman, M., Di Lorenzo, E., Yu, J.-Y., Braconnot, P., Cole, J., Dewitte, B., Giese, B., Guilyardi, E., et al.: Understanding ENSO diversity, *Bull. Amer. Met. Soc.*, 96, 921–938, 2015.
- Compo, G. P. and Sardeshmukh, P. D.: Storm track predictability on seasonal and decadal scales, *J. Climate*, 17, 3701–3720, 2004.
- Cooper, O. R., Langford, A. O., Parrish, D. D., and Fahey, D. W.: Challenges of a lowered US ozone standard, *Science*, 348, 1096–1097, 2015. 410
- Dee, D. P., Uppala, S. M., Simmons, A., Berrisford, P., Poli, P., Kobayashi, S., Andrae, U., Balmaseda, M., Balsamo, G., Bauer, d. P., et al.:



- 415 The ERA-Interim reanalysis: Configuration and performance of the data assimilation system, *Quart. J. R. Met. Soc.*, 137, 553–597, 2011.
- DeFlorio, M. J., Waliser, D. E., Guan, B., Lavers, D. A., Ralph, F. M., and Vitart, F.: Global assessment of atmospheric river prediction skill, *J. Hydrometeor.*, 19, 409–426, 2018.
- DeFlorio, M. J., Waliser, D. E., Guan, B., Ralph, F. M., and Vitart, F.: Global evaluation of atmospheric river subseasonal prediction skill, *Climate Dynamics*, 52, 3039–3060, 2019.
- 420 EPA, U.: Air quality criteria for ozone and related photochemical oxidants, Office, NC f. EA-R., Ed. US EPA: Research Triangle Park, 2, 2006.
- Feldstein, S. B.: The timescale, power spectra, and climate noise properties of teleconnection patterns, *J. Climate*, 13, 4430–4440, 2000.
- 425 Fiore, A., Jacob, D. J., Liu, H., Yantosca, R. M., Fairlie, T. D., and Li, Q.: Variability in surface ozone background over the United States: Implications for air quality policy, *J. Geophys. Res.*, 108, 2003.
- Fiore, A., Oberman, J., Lin, M., Zhang, L., Clifton, O., Jacob, D. J., Naik, V., Horowitz, L., Pinto, J., and Milly, G.: Estimating North American background ozone in US surface air with two independent global models: Variability, uncertainties, and recommendations, *Atm. Environment*, 96, 284–300, 2014.
- 430 Gershunov, A., Shulgina, T., Ralph, F. M., Lavers, D. A., and Rutz, J. J.: Assessing the climate-scale variability of atmospheric rivers affecting western North America, *Geophys. Res. Lett.*, 44, 7900–7908, 2017.
- Guan, B. and Waliser, D. E.: Detection of atmospheric rivers: Evaluation and application of an algorithm for global studies, *J. Geophys. Res.*, 120, 12 514–12 535, 2015.
- Guan, B., Waliser, D. E., Molotch, N. P., Fetzner, E. J., and Neiman, P. J.: Does the Madden–Julian oscillation influence wintertime atmospheric rivers and snowpack in the Sierra Nevada?, *Mon. Wea. Rev.*, 140, 325–342, 2012.
- 435 Guirguis, K., Gershunov, A., Shulgina, T., Clemesha, R. E., and Ralph, F. M.: Atmospheric rivers impacting Northern California and their modulation by a variable climate, *Clim. Dyn.*, 52, 6569–6583, 2019.
- Hitchman, M. H. and Huesmann, A. S.: A seasonal climatology of Rossby wave breaking in the 320–2000-K layer, *J. Atmos. Sci.*, 64, 1922–1940, 2007.
- 440 Hoerling, M. P., Schaack, T. K., and Lenzen, A. J.: A global analysis of stratospheric-tropospheric exchange during northern winter, *Mon. Wea. Rev.*, 121, 162–172, 1993.
- Hollander, M., Wolfe, D. A., and Chicken, E.: *Nonparametric statistical methods*, vol. 751, John Wiley & Sons, 2013.
- Hollingsworth, A., Arpe, K., Tiedtke, M., Capaldo, M., and Savijärvi, H.: The performance of a medium-range forecast model in winter impact of physical parameterizations, *Mon. Wea. Rev.*, 108, 1736–1773, 1980.
- 445 Hoskins, B. and Hodges, K.: The annual cycle of Northern Hemisphere storm tracks. Part I: Seasons, *J. Climate*, 32, 1743–1760, 2019.



- Hoskins, B. J. and Ambrizzi, T.: Rossby wave propagation on a realistic longitudinally varying flow, *J. Atmos. Sci.*, **50**, 1661–1671, 1993.
- Johansson, Å.: Prediction skill of the NAO and PNA from daily to seasonal time scales, *J. Climate*, **20**, 1957–1975, 2007.
- Kim, H.-M. and Alexander, M. A.: ENSO’s modulation of water vapor transport over the Pacific–North American region, *J. Climate*, **28**, 3846–3856, 2015.
- 450
- Knippertz, P. and Wernli, H.: A Lagrangian climatology of tropical moisture exports to the Northern Hemispheric extratropics, *J. Climate*, **23**, 987–1003, 2010.
- Knippertz, P., Wernli, H., and Gläser, G.: A global climatology of tropical moisture exports, *J. Climate*, **26**, 3031–3045, 2013.
- 455 Koch, P., Wernli, H., and Davies, H. C.: An event-based jet-stream climatology and typology, *Int. J. Climatol.*, **26**, 283–301, 2006.
- Kumar, A., Barnston, A. G., Peng, P., Hoerling, M. P., and Goddard, L.: Changes in the spread of the variability of the seasonal mean atmospheric states associated with ENSO, *J. Climate*, **13**, 3139–3151, 2000.
- Kumar, A., Jha, B., Zhang, Q., and Bounoua, L.: A new methodology for estimating the unpredictable component of seasonal atmospheric variability, *J. Climate*, **20**, 3888–3901, 2007.
- 460
- Langford, A.: Stratosphere-troposphere exchange at the subtropical jet: Contribution to the tropospheric ozone budget at midlatitudes, *Geophys. Res. Lett.*, **26**, 2449–2452, 1999.
- Langford, A. and Reid, S.: Dissipation and mixing of a small-scale stratospheric intrusion in the upper troposphere, *J. Geophys. Res.*, **103**, 31 265–31 276, 1998.
- 465 Langford, A., O’Leary, T., Masters, C., Aikin, K., and Proffitt, M.: Modulation of middle and upper tropospheric ozone at northern midlatitudes by the El Niño/Southern Oscillation, *Geophys. Res. Lett.*, **25**, 2667–2670, 1998.
- Langford, A., Aikin, K., Eubank, C., and Williams, E.: Stratospheric contribution to high surface ozone in Colorado during springtime, *Geophys. Res. Lett.*, **36**, 2009.
- Lavers, D. A., Pappenberger, F., and Zsoter, E.: Extending medium-range predictability of extreme hydrological events in Europe, *Nat. Commun.*, **5**, 1–7, 2014.
- 470
- Lavers, D. A., Waliser, D. E., Ralph, F. M., and Dettinger, M. D.: Predictability of horizontal water vapor transport relative to precipitation: Enhancing situational awareness for forecasting western US extreme precipitation and flooding, *Geophys. Res. Lett.*, **43**, 2275–2282, 2016.
- Lee, S.-K., Mapes, B. E., Wang, C., Enfield, D. B., and Weaver, S. J.: Springtime ENSO phase evolution and its relation to rainfall in the continental US, *Geophys. Res. Lett.*, **41**, 1673–1680, 2014.
- 475



- Lefohn, A. S., Wernli, H., Shadwick, D., Limbach, S., Oltmans, S. J., and Shapiro, M.: The importance of stratospheric–tropospheric transport in affecting surface ozone concentrations in the western and northern tier of the United States, *Atm. Environment*, 45, 4845–4857, 2011.
- 480 Lin, M., Fiore, A. M., Horowitz, L. W., Langford, A. O., Oltmans, S. J., Tarasick, D., and Rieder, H. E.: Climate variability modulates western US ozone air quality in spring via deep stratospheric intrusions, *Nat. Commun.*, 6, 2015.
- Madonna, E., Wernli, H., Joos, H., and Martius, O.: Warm conveyor belts in the ERA-Interim dataset (1979–2010). Part I: Climatology and potential vorticity evolution, *J. Climate*, 27, 3–26, 2014.
- Mahoney, K., Jackson, D. L., Neiman, P., Hughes, M., Darby, L., Wick, G., White, A., Sukovich, E., and Cifelli, R.:
485 Understanding the role of atmospheric rivers in heavy precipitation in the southeast United States, *Mon. Wea. Rev.*, 144, 1617–1632, 2016.
- Marsaglia, G., Tsang, W. W., Wang, J., et al.: Evaluating Kolmogorov’s distribution, *J. Stat. Softw.*, 8, 1–4, 2003.
- Monahan, A. H., Fyfe, J. C., Ambaum, M. H., Stephenson, D. B., and North, G. R.: Empirical orthogonal functions: The medium is the message, *J. Climate*, 22, 6501–6514, 2009.
- 490 Monhart, S., Spirig, C., Bhend, J., Bogner, K., Schär, C., and Liniger, M. A.: Skill of subseasonal forecasts in Europe: Effect of bias correction and downscaling using surface observations, *J. Geophys. Res.*, 123, 7999–8016, 2018.
- Mundhenk, B. D., Barnes, E. A., and Maloney, E. D.: All-season climatology and variability of atmospheric river frequencies over the North Pacific, *J. Climate*, 29, 4885–4903, 2016.
- 495 Mundhenk, B. D., Barnes, E. A., Maloney, E. D., and Baggett, C. F.: Skillful empirical subseasonal prediction of landfalling atmospheric river activity using the Madden–Julian oscillation and quasi-biennial oscillation, *NPJ Climate and Atmospheric Science*, 1, 1–7, 2018.
- Murphy, A. H. and Epstein, E. S.: Skill scores and correlation coefficients in model verification, *Mon. Wea. Rev.*, 117, 572–582, 1989. Nakamura, H.: Midwinter suppression of baroclinic wave activity in the Pacific, *J. Atmos. Sci.*, 49, 1629–1642, 1992.
- 500 Newman, M. and Sardeshmukh, P. D.: The impact of the annual cycle on the North Pacific/North American response to remote low-frequency forcing, *J. Atmos. Sci.*, 55, 1336–1353, 1998.
- Newman, M., Kiladis, G. N., Weickmann, K. M., Ralph, F. M., and Sardeshmukh, P. D.: Relative contributions of synoptic and low-frequency eddies to time-mean atmospheric moisture transport, including the role of atmospheric rivers, *J. Climate*, 25, 7341–7361, 2012.
- 505 North, G. R., Bell, T. L., Cahalan, R. F., and Moeng, F. J.: Sampling errors in the estimation of empirical orthogonal functions, *Mon. Wea. Rev.*, 110, 699–706, 1982.
- Olsen, M. A., Manney, G. L., and Liu, J.: The ENSO and QBO Impact on Ozone Variability and Stratosphere-Troposphere Exchange Relative to the Subtropical Jets, *J. Geophys. Res.*, 124, 7379–7392, 2019.



- Pan, B., Hsu, K., AghaKouchak, A., Sorooshian, S., and Higgins, W.: Precipitation prediction skill for the West Coast United States: From short to extended range, *J. Climate*, 32, 161–182, 2019.
- 510 Pavan, V., Tibaldi, S., and Branković, Č.: Seasonal prediction of blocking frequency: Results from winter ensemble experiments, *Quart. J. R. Met. Soc.*, 126, 2125–2142, 2000.
- Penland, C. and Matrosova, L.: Studies of El Nino and interdecadal variability in tropical sea surface temperatures using a nonnormal filter, *J. Climate*, 19, 5796–5815, 2006.
- 515 Pfahl, S., Madonna, E., Boettcher, M., Joos, H., and Wernli, H.: Warm conveyor belts in the ERA-Interim dataset (1979–2010). Part II: Moisture origin and relevance for precipitation, *J. Climate*, 27, 27–40, 2014.
- Ralph, F. and Dettinger, M.: Storms, floods, and the science of atmospheric rivers, *EOS*, 92, 265–266, 2011.
- Reed, R. J. and Danielsen, E. F.: Fronts in the vicinity of the tropopause, *Arch. Met. Geoph. Biokl. A*, 11, 1–17, 1958.
- Rivière, G.: Role of Rossby wave breaking in the west Pacific teleconnection, *Geophys. Res. Lett.*, 37, 2010.
- 520 Ryoo, J.-M., Kaspi, Y., Waugh, D. W., Kiladis, G. N., Waliser, D. E., Fetzer, E. J., and Kim, J.: Impact of Rossby wave breaking on US West Coast winter precipitation during ENSO events, *J. Climate*, 26, 6360–6382, 2013.
- Schwierz, C., Dirren, S., and Davies, H. C.: Forced waves on a zonally aligned jet stream, *J. Atmos. Sci.*, 61, 73–87, 2004.
- Scott, R. and Cammas, J.: Wave breaking and mixing at the subtropical tropopause, *J. Atmos. Sci.*, 59, 2347–2361, 2002.
- Seidel, D. J., Zhang, Y., Beljaars, A., Golaz, J.-C., Jacobson, A. R., and Medeiros, B.: Climatology of the planetary boundary layer over the continental United States and Europe, *J. Geophys. Res.*, 117, 2012.
- 525 Shapiro, M.: Turbulent mixing within tropopause folds as a mechanism for the exchange of chemical constituents between the stratosphere and troposphere, *J. Atmos. Sci.*, 37, 994–1004, 1980.
- Shapiro, M. A. and Keyser, D.: Fronts, jet streams and the tropopause, in: *Extratropical Cyclones. The Erik Palmén Memorial Volume*, pp. 167–191, American Meteorological Society, 1990.
- 530 Škerlak, B., Sprenger, M., and Wernli, H.: A global climatology of stratosphere–troposphere exchange using the ERA-Interim data set from 1979 to 2011, *Atmos. Chem. Phys.*, 14, 913–937, 2014.
- Škerlak, B., Sprenger, M., Pfahl, S., Tyrlis, E., and Wernli, H.: Tropopause folds in ERA-Interim: Global climatology and relation to extreme weather events, *J. Geophys. Res.*, 120, 4860–4877, 2015.
- Sprenger, M. and Wernli, H.: The LAGRANTO Lagrangian analysis tool—version 2.0, *Geosci. Model Dev*, 8, 2569–2586, 2015.
- 535 Sprenger, M., Maspoli, M. C., and Wernli, H.: Tropopause folds and cross-tropopause exchange: A global investigation based upon ECMWF analyses for the time period March 2000 to February 2001, *J. Geophys. Res.*, 108, 2003.



- Sprenger, M., Fragkoulidis, G., Binder, H., Croci-Maspoli, M., Graf, P., Grams, C. M., Knippertz, P., Madonna, E., Schemm, S., Škerlak, B., et al.: Global climatologies of Eulerian and Lagrangian flow features based on ERA-Interim, *Bull. Amer. Met. Soc.*, 98, 1739–1748, 2017.
- 540 Stohl, A. and James, P.: A Lagrangian Analysis of the Atmospheric Branch of the Global Water Cycle. Part II: Moisture Transports between Earth’s Ocean Basins and River Catchments, *J. Hydrometeor.*, 6, 961–984, 2005.
- Straus, D., Shukla, J., Paolino, D., Schubert, S., Suarez, M., Pegion, P., and Kumar, A.: Predictability of the seasonal mean atmospheric circulation during autumn, winter, and spring, *J. Climate*, 16, 3629–3649, 2003.
- Straus, D. M. and Shukla, J.: Does ENSO force the PNA?, *J. Climate*, 15, 2340–2358, 2002.
- 545 Van Den Dool, H. M. and Toth, Z.: Why do forecasts for “near normal” often fail?, *Wea. Forecasting*, 6, 76–85, 1991.
- Vitart, F., Ardilouze, C., Bonet, A., Brookshaw, A., Chen, M., Codorean, C., Déqué, M., Ferranti, L., Fucile, E., Fuentes, M., et al.: The subseasonal to seasonal (S2S) prediction project database, *Bull. Amer. Meteor. Soc.*, 98, 163–173, 2017.
- Wang, L. and Robertson, A. W.: Week 3–4 predictability over the United States assessed from two operational ensemble prediction systems, *Climate Dynamics*, 52, 5861–5875, 2019.
- 550 Wernli, B. H. and Davies, H. C.: A Lagrangian-based analysis of extratropical cyclones. I: The method and some applications, *Quart. J. R. Met. Soc.*, 123, 467–489, 1997.
- Wernli, H. and Bourqui, M.: A Lagrangian “1-year climatology” of (deep) cross-tropopause exchange in the extratropical Northern Hemisphere, *J. Geophys. Res.*, 107, ACL–13, 2002.
- Wernli, H. and Sprenger, M.: Identification and ERA-15 climatology of potential vorticity streamers and cutoffs near the extratropical tropopause, *J. Atmos. Sci.*, 64, 1569–1586, 2007.
- 555 Wu, R. and Kirtman, B. P.: Changes in spread and predictability associated with ENSO in an ensemble coupled GCM, *J. Climate*, 19, 4378–4396, 2006.
- Yamagami, A. and Matsueda, M.: Subseasonal Forecast Skill for Weekly Mean Atmospheric Variability Over the Northern Hemisphere in Winter and Its Relationship to Midlatitude Teleconnections, *Geophys. Res. Lett.*, 47, e2020GL088 508, 2020.
- 560 Younas, W. and Tang, Y.: PNA predictability at various time scales, *J. Climate*, 26, 9090–9114, 2013.
- Young, P. J., Naik, V., Fiore, A. M., Gaudel, A., Guo, J., Lin, M., Neu, J., Parrish, D., Reider, H., Schnell, J., et al.: Tropospheric Ozone Assessment Report: Assessment of global-scale model performance for global and regional ozone distributions, variability, and trends, *Elem. Sci. Anth.*, 6, 2018.
- 565 Zhu, Y. and Newell, R. E.: A proposed algorithm for moisture fluxes from atmospheric rivers, *Mon. Wea. Rev.*, 126, 725–735, 1998.



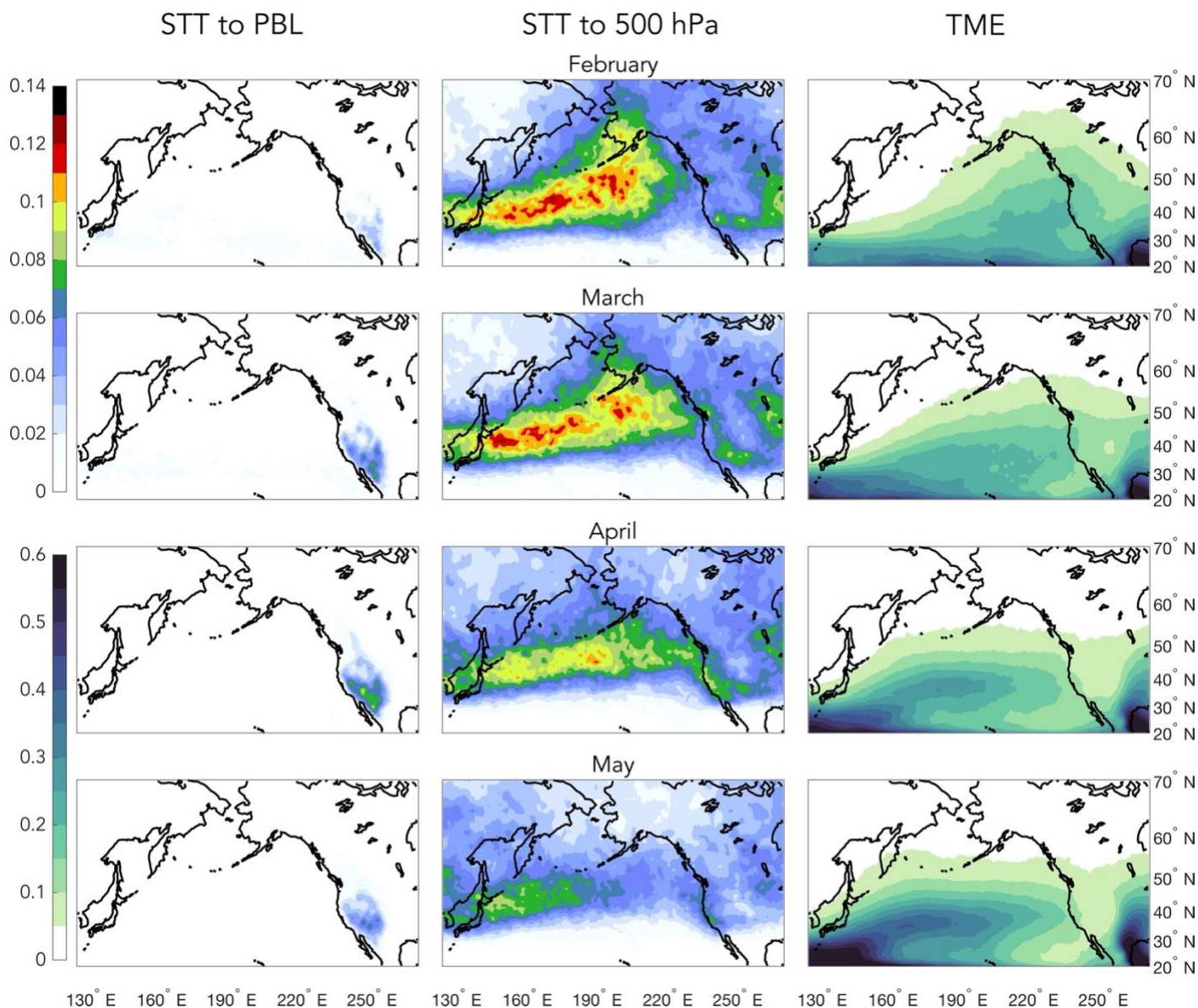
	WP	PNA	ONI
PC1	-0.66 (0.00)	0.44 (0.00)	0.16 (0.1)
PC2	-0.38 (0.00)	-0.09 (0.35)	-0.78 (0.00)
PC3	-0.31 (0.00)	-0.56 (0.00)	-0.05 (0.64)

570 **Table 1:** Correlations between MAM monthly average PC time series and various climate indices, with p-values in parentheses. The West Pacific pattern (WP) and Pacific-North American pattern (PNA) and NOAA Oceanic Niño Index (ONI) are taken from NOAA Center for Weather and Climate Prediction (NOAA CPC).



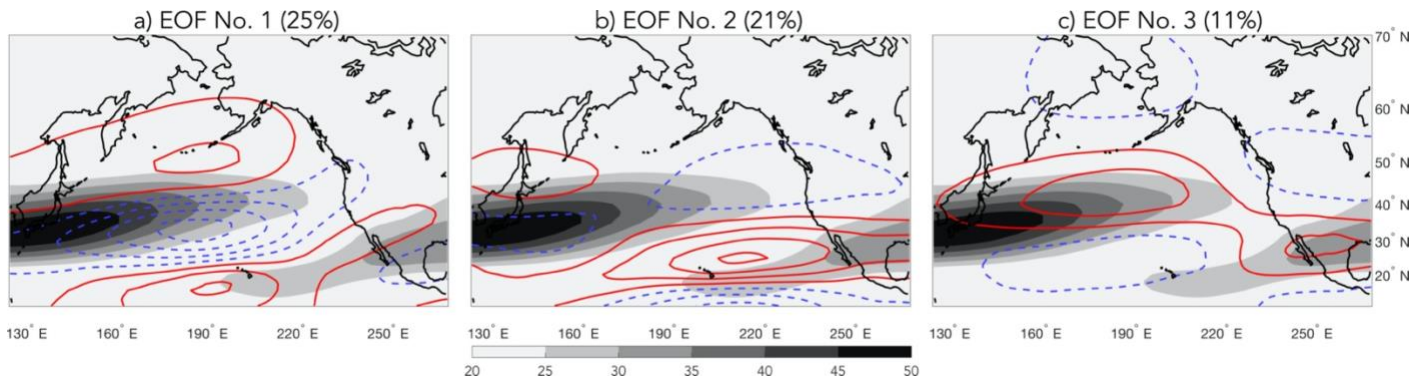
	<i>week 1</i>	<i>week 2</i>	<i>week 3</i>	<i>week 4</i>	<i>week 5</i>	<i>week 6</i>
PC 1	0.96	0.78	0.56	0.42	0.3	0.31
PC 2	0.97	0.86	0.73	0.7	0.67	0.66
PC 3	0.94	0.67	0.38	0.21	0.11	0.09

Table 2: Correlations between MAM weekly average PC time series of IFS hindcasts and ERA-Interim verifications.

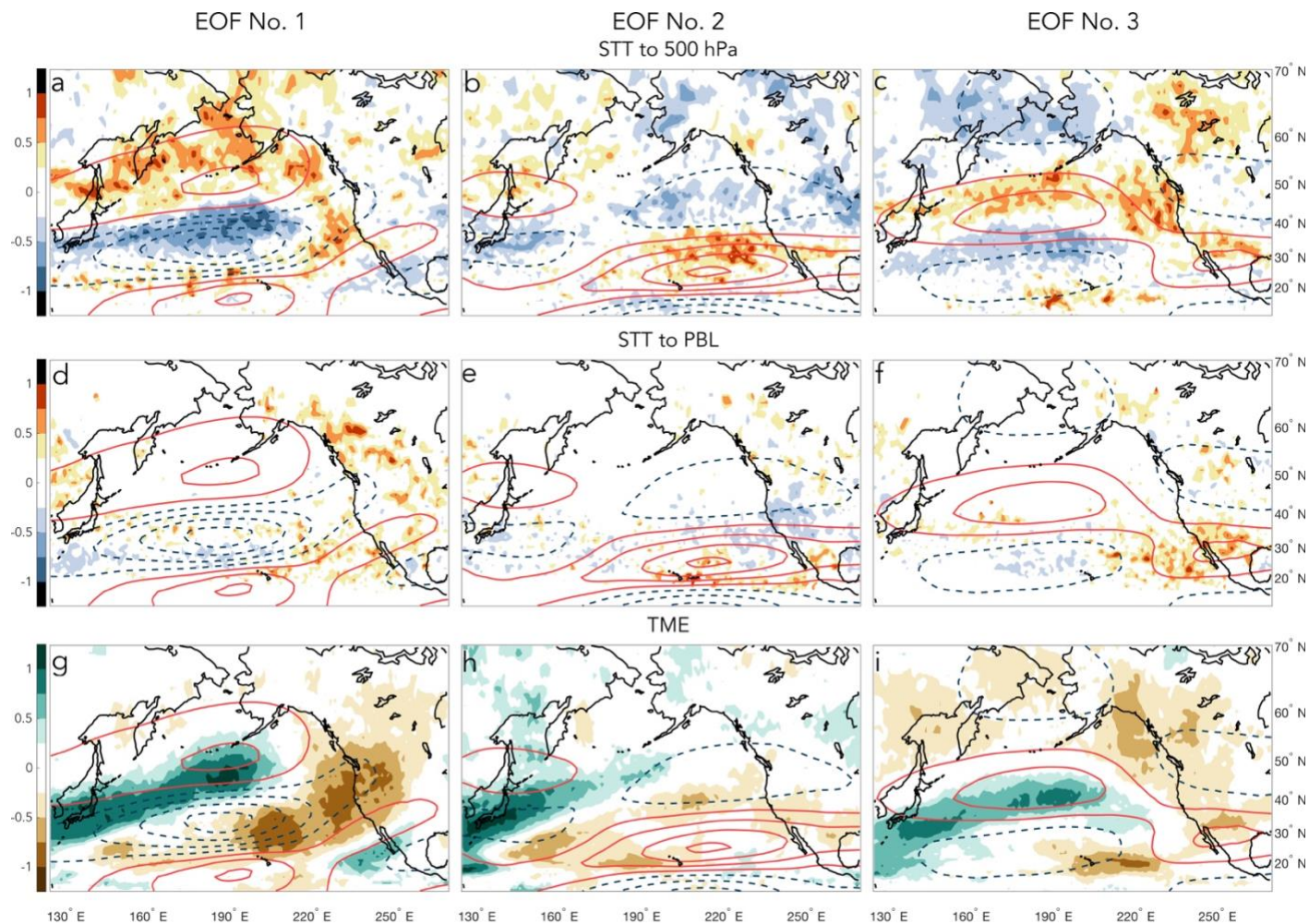


575

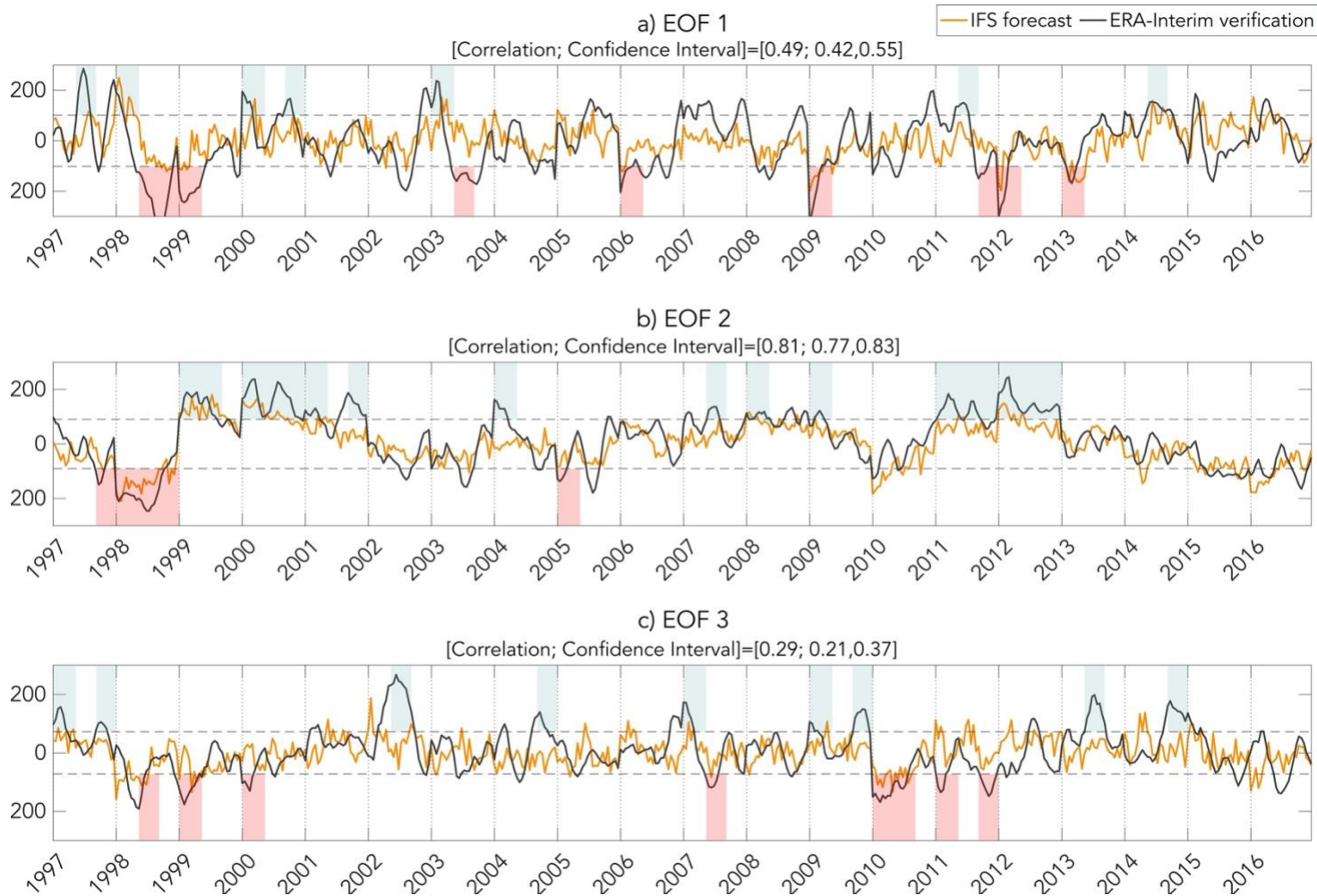
Figure 1: Monthly average climatologies (1979-2014) of STT to the PBL (left column), STT to 500 hPa (middle column), and TME (right column). Units for all panels are event frequencies (events/6-hourly time step), where each of the relevant events types are defined in Sect. 2.2.



580 **Figure 2:** Spring (MAM, 1979-2014) zonal wind climatology (filled contours) with colored contours showing the first three EOF patterns. The variance explained by each EOF is shown in the title for each panel.



585 **Figure 3:** Monthly mean (MAM, 1979-2014) frequencies (filled contours) of STT to 500 hPa (top row), STT to the PBL (middle row), and TME (bottom row), for time periods when PCs 1-3 are greater than ± 1 STDs from climatology (units of STDs). Colored contours show the EOF patterns associated with each composite.



590

Figure 4: Time series of weeks 3-5 average zonal wind projected onto EOFs 1-3 for IFS forecasts (orange lines) and ERA-Interim verifications (black lines). The horizontal dashed lines denote ± 0.8 STDs from the mean of the verification time series. For reference, the light blue and red shading denote the months that were included in the monthly average composites used to create Fig. 3. Correlations between the forecasts and verifications (with 95th percentile confidence intervals) are shown in the titles of each panel.

595

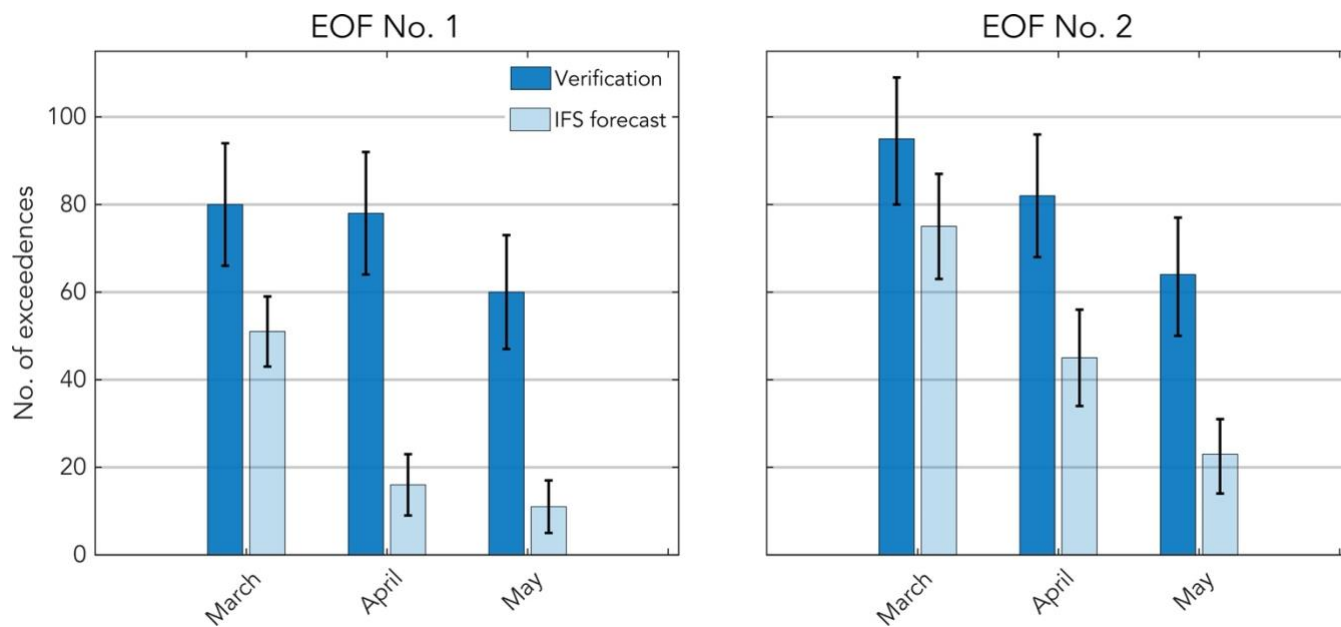
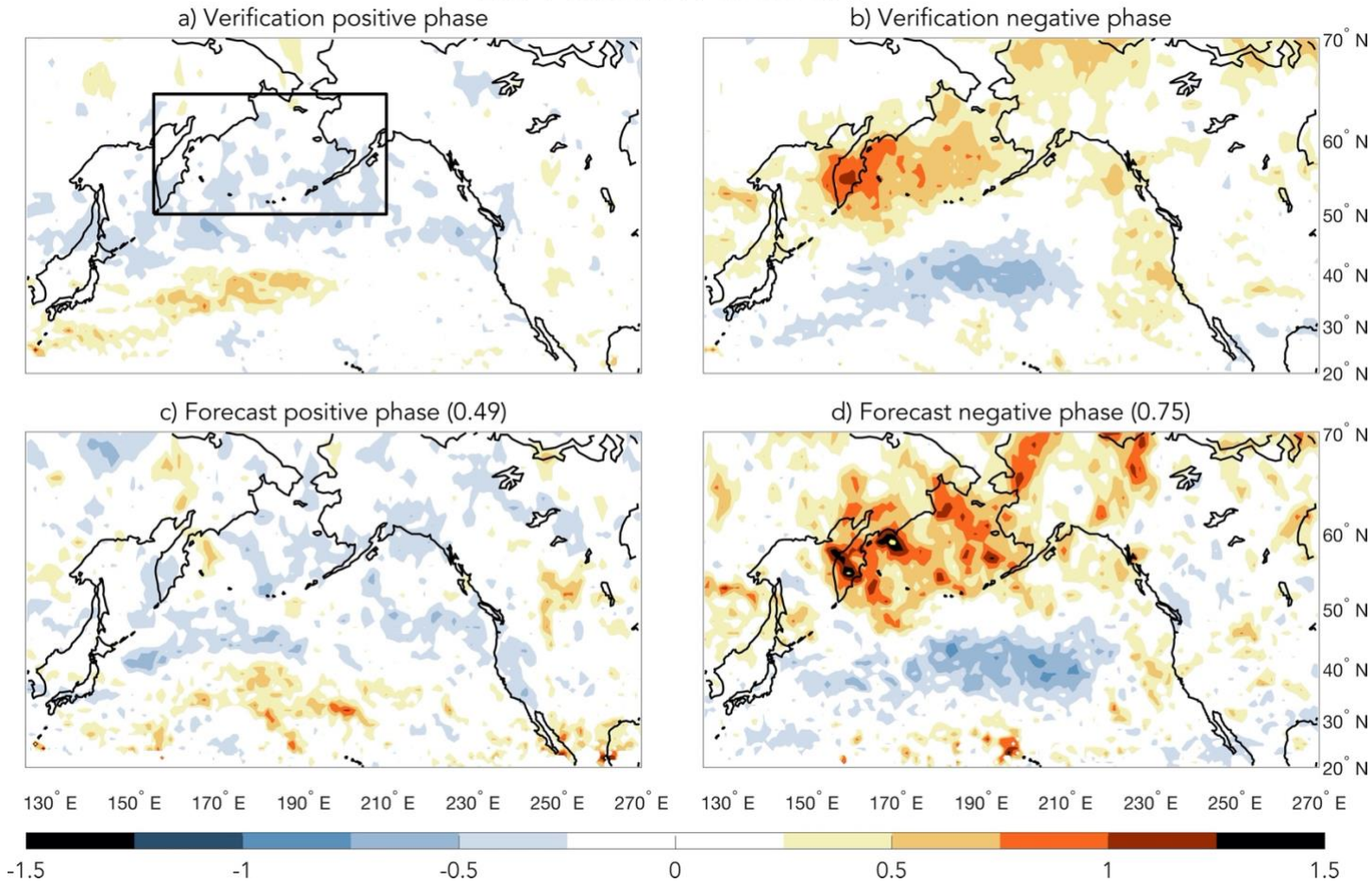


Figure 5: Number of times that a weeks 3-5 average verification or forecast exceeded the 0.8 STD threshold for the 1997-2016 hindcast period (i.e., the periods in Fig. 4 where the black or orange lines, respectively, was above or below the dashed horizontal STD reference lines). 95th percentile bootstrap confidence intervals are shown as whiskers.

600



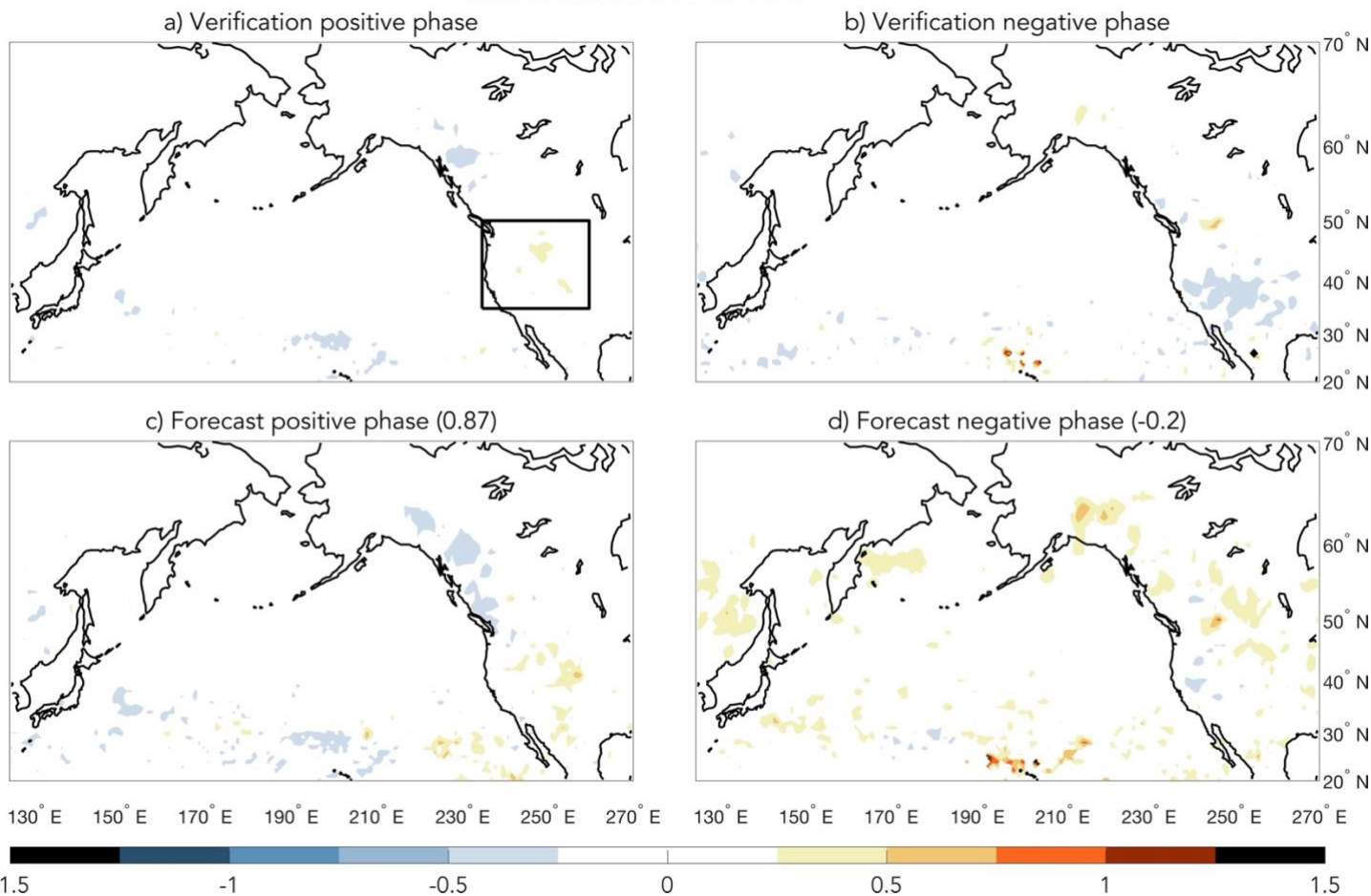
EOF1-based STT to 500 hPa



605 **Figure 6:** (a), (b) EOF1-based composites of STT to 500 hPa for weeks 3-5 forecast periods when the verification time series (black line in Fig. 4) was above (positive phase) or below (negative phase) the 0.8 STD threshold. (c), (d) EOF1-based composites of STT to 500 hPa for weeks 3-5 forecast periods when the forecast time series (orange line in Fig. 4) was above (positive phase) or below (negative phase) the 0.8 STD threshold. The black box outlines the North Pacific subregion used for creating the transport PDF in Fig. 10a. Units are in STDs and pattern correlations between top and bottom panels (cf., (a) versus (c) and (b) versus (d)) are shown in the bottom row titles.



EOF2-based STT to PBL



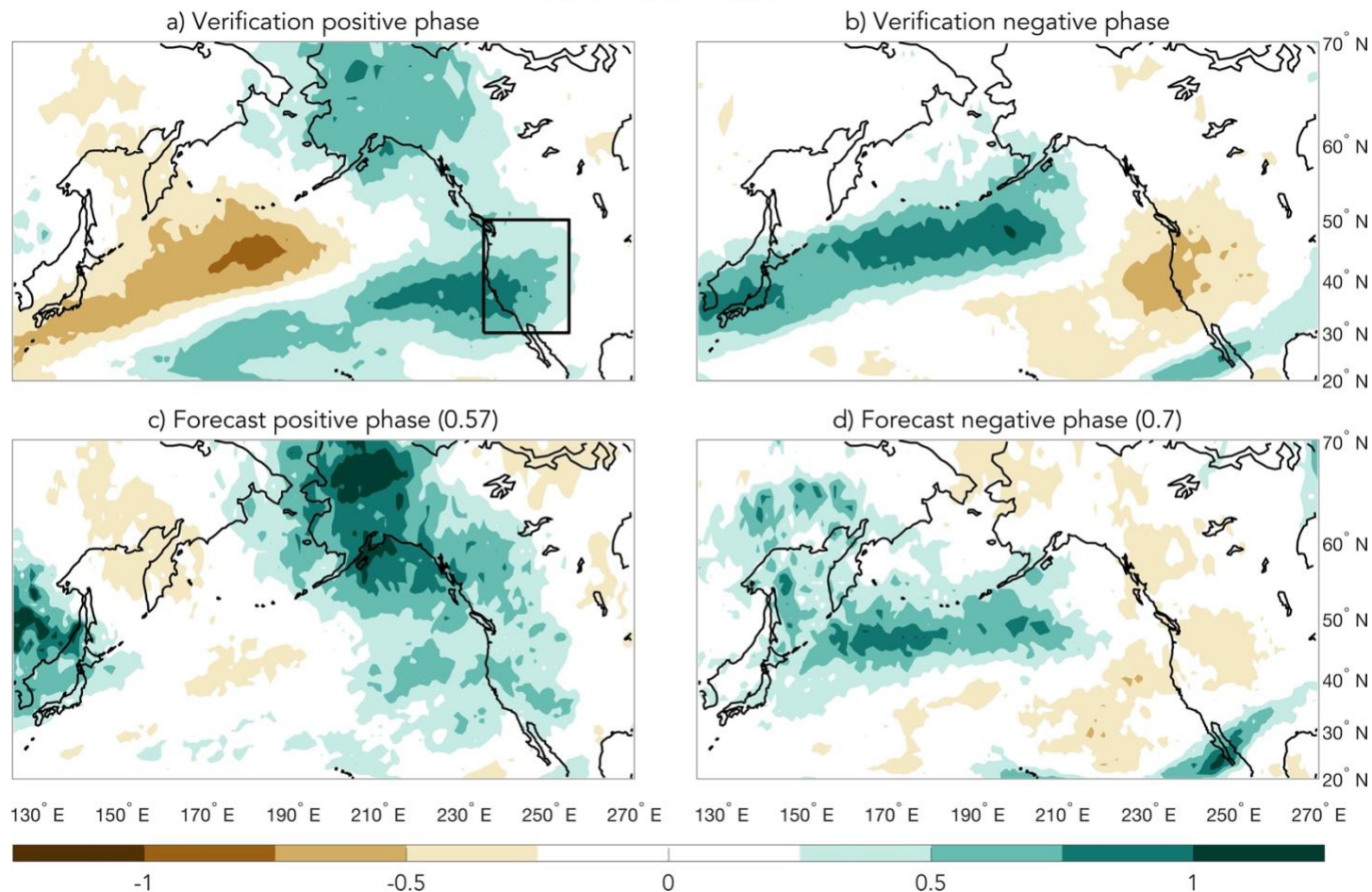
610

Figure 7: (a), (b) EOF2-based composites of STT to the PBL for weeks 3-5 forecast periods when the verification time series (black line in Fig. 4) was above (positive phase) or below (negative phase) the 0.8 STD threshold. (c), (d) EOF2-based composites of STT to the PBL for weeks 3-5 forecast periods when the forecast time series (orange line in Fig. 4) was above (positive phase) or below (negative phase) the 0.8 STD threshold. The black box outlines the western to intermountain-western US subregion used for creating the transport PDF in Fig. 10b. Units are in STDs and pattern correlations between top and bottom panels (cf., (a) versus (c) and (b) versus (d)) are shown in the bottom row titles.

615



EOF1-based TME

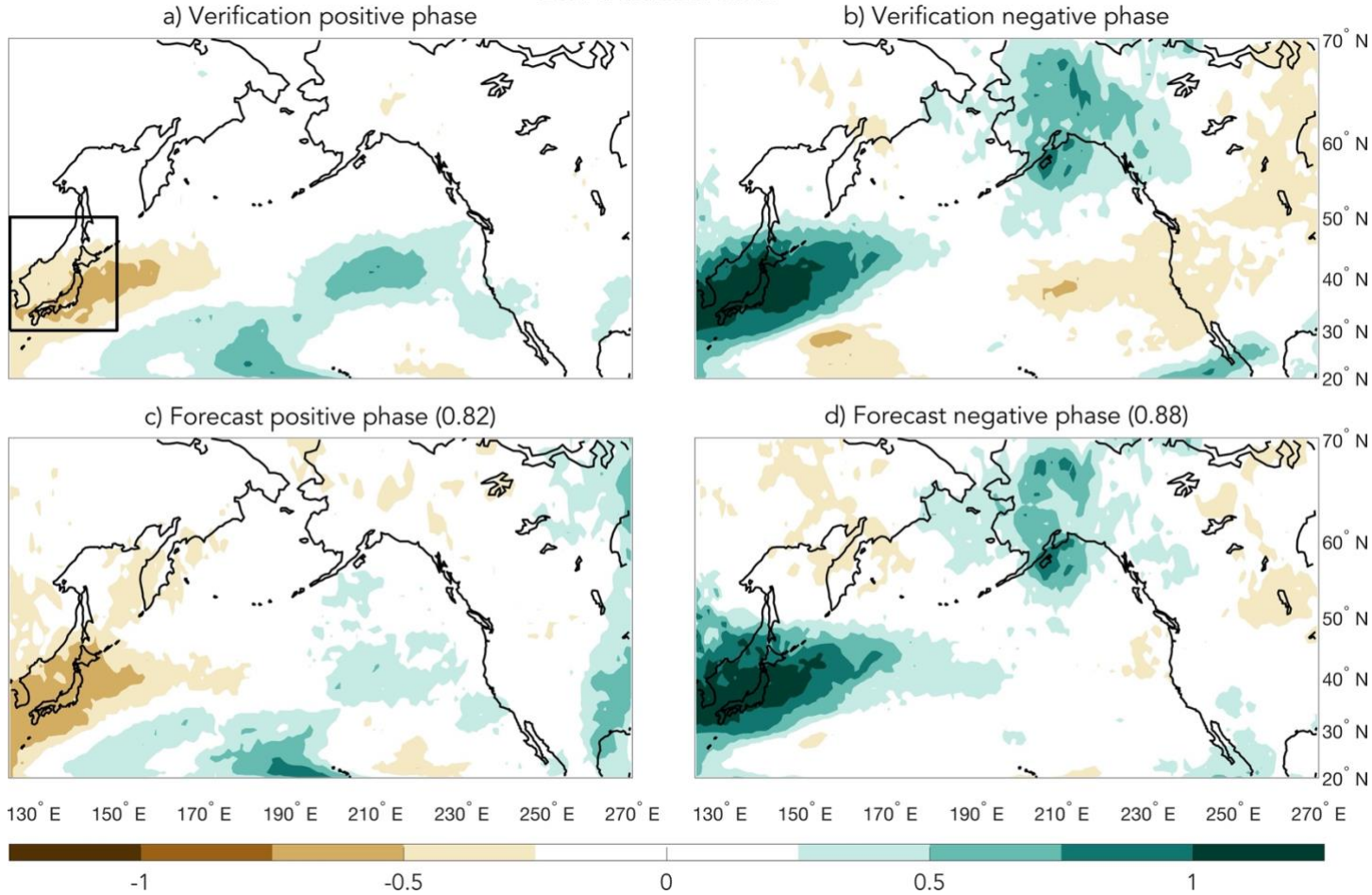


620 **Figure 8:** (a), (b) EOF1-based composites of TME for weeks 3-5 forecast periods when the verification time series (black line in Fig. 4) was above (positive phase) or below (negative phase) the 0.8 STD threshold. (c), (d) EOF1-based composites of TME for weeks 3-5 forecast periods when the forecast time series (orange line in Fig. 4) was above (positive phase) or below (negative phase) the 0.8 STD threshold. The black box outlines the western US subregion used for creating the transport PDF in Fig. 10c. Units are in STDs and pattern correlations between top and bottom panels (cf., (a) versus (c) and (b) versus (d)) are shown in the bottom row titles.

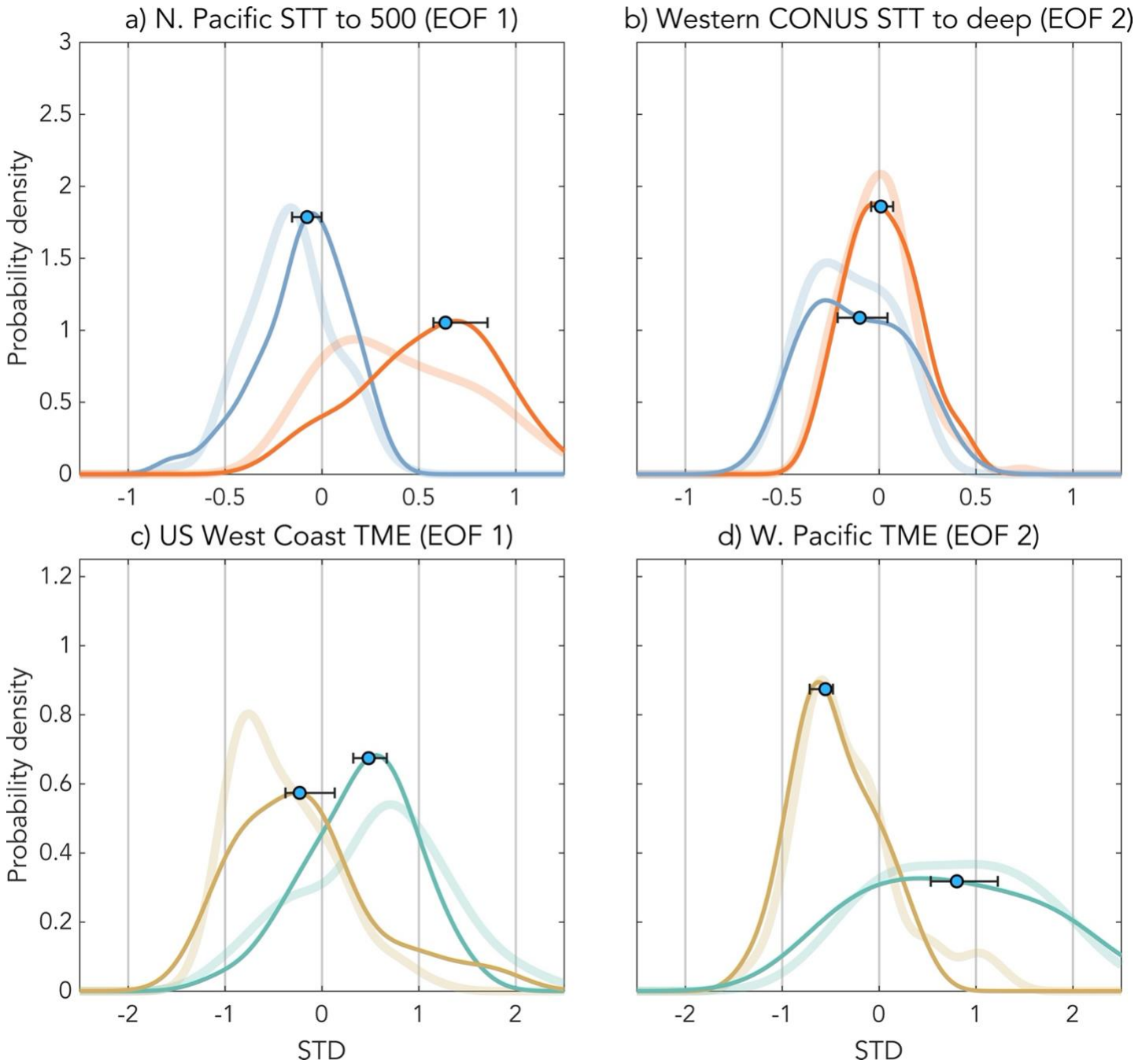
625



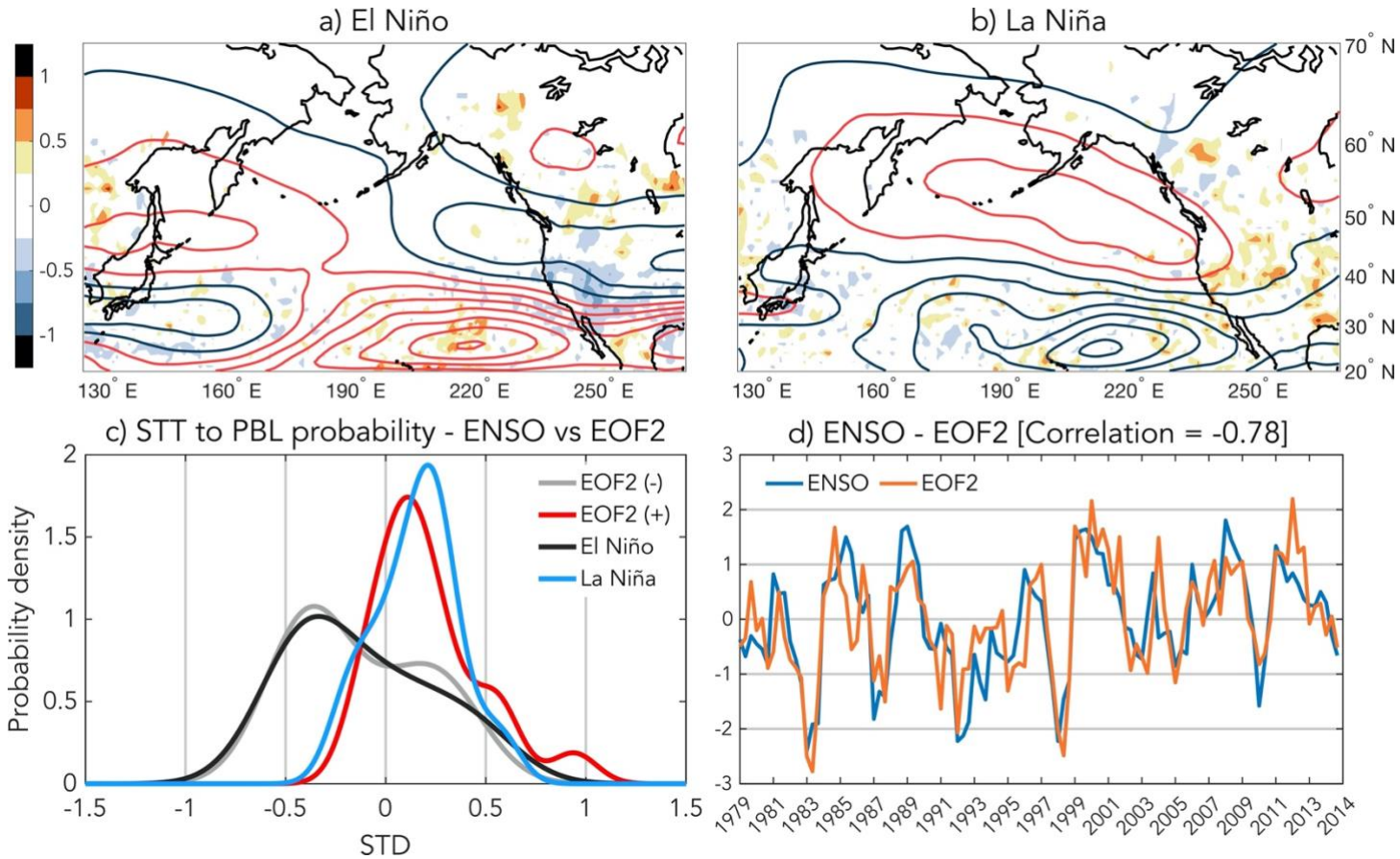
EOF2-based TME



630 **Figure 9:** (a), (b) EOF2-based composites of TME for weeks 3-5 forecast periods when the verification time series (black line in Fig. 4) was above (positive phase) or below (negative phase) the 0.8 STD threshold. (c), (d) EOF2-based composites of TME for weeks 3-5 forecast periods when the forecast time series (orange line in Fig. 4) was above (positive phase) or below (negative phase) the 0.8 STD threshold. The black box outlines the West Pacific subregion used for creating the transport PDF in Fig. 10d. Units are in STDs and pattern correlations between top and bottom panels (cf., (a) versus (c) and (b) versus (d)) are shown in the bottom row titles.



635 **Figure 10:** Probability density functions (PDFs) of (a) EOF1-based STT to 500hPa for the North Pacific subregion, (b) EOF2-based STT to the PBL for the western to intermountain-western US subregion, (c) EOF1-based TME to the western US subregion, and (d) EOF2-based TME to the West Pacific subregion. IFS-based forecasts are shown in solid dark lines (with medians shown as blue dots and 95th percentile bootstrap confidence intervals shown as whiskers) and ERA-Interim-based verifications are shown as thicker light lines. Units are in STDs.



640 **Figure 11:** (a) El Niño- and (b) La Niña-based monthly mean (MAM, 1979-2014) frequencies of STT to the PBL (filled contours) and zonal winds (contours) for time periods when the NOAA ONI was +/-0.8 STDs from climatology (units of STDs). Note: for correct comparison, panels (a) should be compared to panels (d) from Fig. 4; compare also panels (a) and (b) here to panels (d) and (c) from Fig. S3. (c) Probability density functions (PDFs) of EOF2-based STT to the PBL for the western to intermountain-western US subregion. (d) Time series of the NOAA ONI (blue line) and PC2 (orange line), where ONI has multiplied by -1 for ease of comparison.



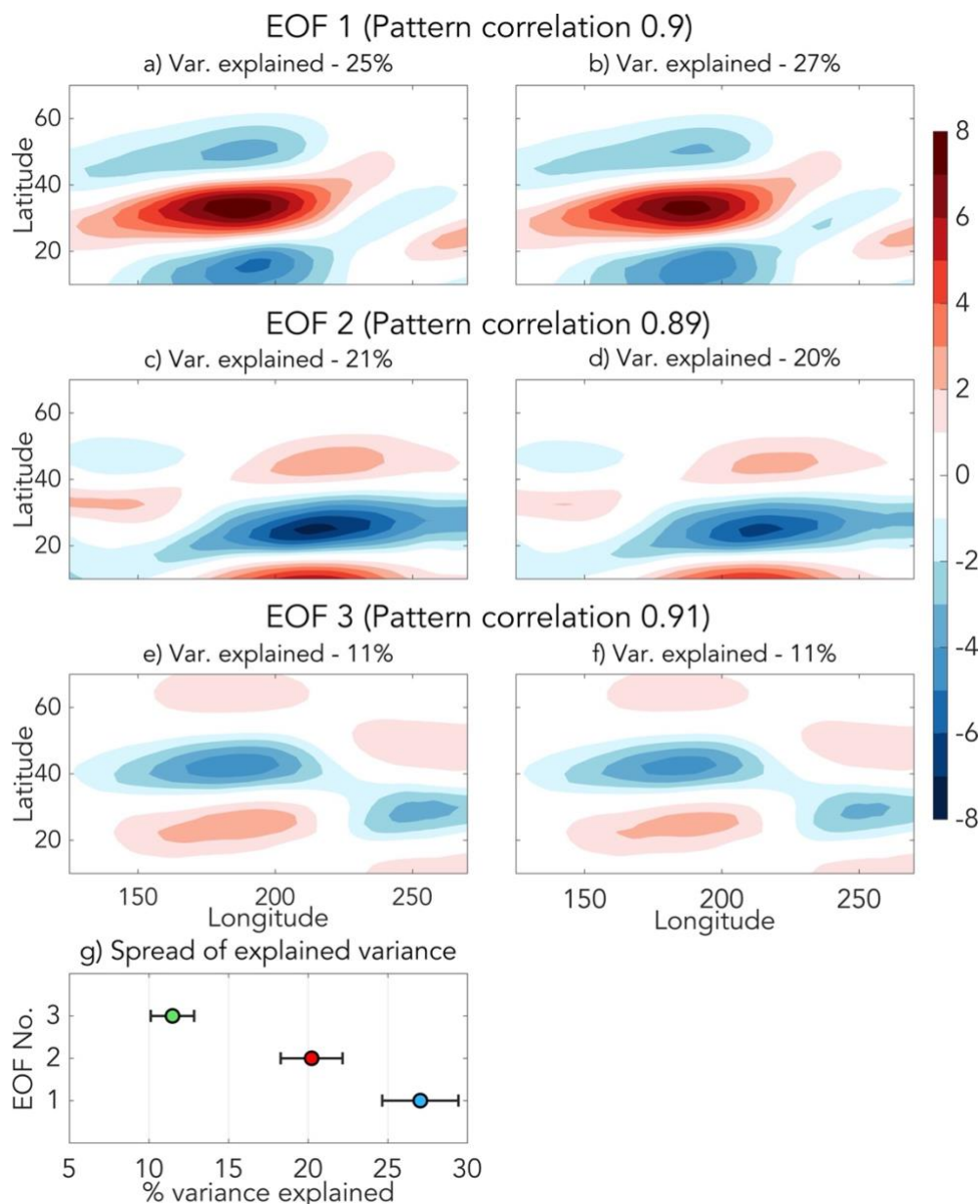
645

Appendix

To verify that EOFs 1-3 represent distinct patterns that are robust to variations in sampling period (North et al. 1982), we conducted several calculations. To begin, a 10,000 member bootstrap ensemble of 200 hPa zonal wind EOFs was created (resampling with replacement), where each bootstrap member consisted of ‘N’ randomly selected monthly mean 200 hPa zonal wind anomalies for the Pacific basin domain shown in Fig. 2. The ‘N’ randomly selected anomalies are chosen from the pool of all MAM 1979-2016 monthly means, and N=114, which is the number of months in the original EOF calculation for MAM, 1979-2016. The resulting data was used in three calculations.

First, the pattern correlation between each bootstrap ensemble member EOF and the corresponding original EOF was calculated. The median pattern correlation for all 10,000 bootstrap ensemble members was then calculated. For all three EOFs, the median pattern correlation was near 0.9 (individual values are shown for each of the three EOFs in the title bars of Fig. A1 a-f). Next, the median of the variance explained was calculated for each bootstrap ensemble EOF. For all three EOFs, the variance explained for the original EOFs and for the median of the bootstrap ensemble EOFs is within a couple percent (individual values are shown for each of the EOFs in the title bars of Fig. A1 a-f). And finally, the standard deviation of the variance explained was calculated for each of the bootstrap ensembles (Fig. A1g). The spread (measured by the standard deviation) is small enough that there is no overlap between each of the first three EOFs. In combination, these calculations support the notion that the first three 200 hPa zonal wind EOFs are not degenerate according to the criteria outlined in North et al. 1982.

665



670 Figure A1: (a), (c), and (e) 200 hPa zonal wind EOF patterns for MAM, 1979-2016, which correspond to the EOF contours shown in Figs. 2-3 and S1-S4. (b), (d), and (f) 200 hPa zonal wind EOF patterns for the bootstrap ensembles corresponding to panels (a), (c), and (e), respectively. For each row in (a)-(f), the median pattern correlation between the original (left column) and bootstrap ensembles (right column) are shown in the subtitle. The subtitle of each panel in (a)-(f) also shows the variance explained (original EOFs, left column) or the median variance explained (bootstrap ensembles, right column) for each EOF. (g) Median variance explained for the bootstrap ensemble (solid marker), and the spread of variance explained for the bootstrap ensembles of each EOF, where the spread is calculated as 1 STD of the variance explained (shown as whiskers).